

**Manuscript version: Author's Accepted Manuscript**

The version presented in WRAP is the author's accepted manuscript and may differ from the published version or Version of Record.

**Persistent WRAP URL:**

<http://wrap.warwick.ac.uk/149220>

**How to cite:**

Please refer to published version for the most recent bibliographic citation information. If a published version is known of, the repository item page linked to above, will contain details on accessing it.

**Copyright and reuse:**

The Warwick Research Archive Portal (WRAP) makes this work by researchers of the University of Warwick available open access under the following conditions.

Copyright © and all moral rights to the version of the paper presented here belong to the individual author(s) and/or other copyright owners. To the extent reasonable and practicable the material made available in WRAP has been checked for eligibility before being made available.

Copies of full items can be used for personal research or study, educational, or not-for-profit purposes without prior permission or charge. Provided that the authors, title and full bibliographic details are credited, a hyperlink and/or URL is given for the original metadata page and the content is not changed in any way.

**Publisher's statement:**

Please refer to the repository item page, publisher's statement section, for further information.

For more information, please contact the WRAP Team at: [wrap@warwick.ac.uk](mailto:wrap@warwick.ac.uk).

1 **Effects of particle sphericity and initial fabric on the shearing behavior of soil-**  
2 **rough structural interface**

3 **Wan-Huan Zhou<sup>1</sup>, Xue-Ying Jing<sup>2,\*</sup>, Zhen-Yu Yin<sup>3</sup> and Xueyu Geng<sup>4</sup>**  
4

5 <sup>1</sup> Associate Professor, Department of Civil and Environmental Engineering, Faculty of Science and  
6 Technology, University of Macau, Macau, China and Zhuhai UM Science & Technology Research  
7 Institute, Zhuhai, Guangdong, China  
8

9 <sup>2</sup> PhD, Department of Civil and Environmental Engineering, Faculty of Science and Technology,  
10 University of Macau, Macau, China  
11

12 <sup>3</sup> Associate Professor., Department of Civil and Environmental Engineering, Hong Kong  
13 Polytechnic University, Hung Hom, Kowloon, Hong Kong, China  
14

15 <sup>4</sup> Assistant Professor, Geotechnical Engineering School of Engineering (F332), The University of  
16 Warwick, Coventry, CV4 7AL, UK  
17  
18  
19  
20

21 \*Corresponding author

22 Ph.D.

23 Department of Civil and Environmental Engineering, Faculty of Science and Technology,  
24 University of Macau, Macau, China.

25 Tel: (0086) 138 2801 9916

26 E-mail: jingxueying73@gmail.com  
27  
28  
29

8718 words, 3tables and 24 figures

## 30 **Abstract**

31 In this study, the effects of particle sphericity and initial fabric on the shearing behavior of soil-  
32 structural interface (SSI) were analyzed by discrete element method (DEM). Three types of  
33 clustered particles were designed to represent irregular particles featuring various sphericities. The  
34 extreme porosities of granular materials composed of various clustered particles were affected by  
35 particle sphericity. Moreover, five specimens consisting of differently oriented particles were  
36 prepared to study the effect of initial fabric. A series of interface shear tests (ISTs) featuring varying  
37 interface roughnesses were carried out using three-dimensional (3D) DEM simulations. The macro-  
38 response showed that the shear strength of the interface increased as particle sphericity decreased,  
39 while stress softening and dilatancy were easily observed during the shearing. From the particle-  
40 scale analysis, it was found that the thickness of the localized band was affected by the interface  
41 roughness, the normal stress and the initial fabric while independent of the particle sphericity. The  
42 thickness generally ranged between 4 and 6 times that of the median particle equivalent diameter. A  
43 thicker localized band was formed in the case of rougher interface and in soil composed of inclined  
44 placed and randomly placed particles. The coordination number measured in the interface zone and  
45 upper zone suggested that the dilation mostly occurs inside the interface zone. Anisotropy was  
46 induced by the interface shearing of the initial isotropic specimens. The direction of shear-induced  
47 anisotropy correlates with the shearing direction. The evolutions of anisotropies for the anisotropic  
48 specimens depend on the initial fabric.

49 **Key words:** Discrete element method; soil-structural interface; particle sphericity effect; initial  
50 fabric; interface roughness

## 51 **1. Introduction:**

52 The soil-structural interface (SSI) is involved in many aspects of geotechnical engineering. The  
53 conventional research studies that characterize the mechanical behavior of SSI commonly rely on

54 laboratory-based and on-site experiments. Certain valuable phenomena have been observed and  
55 have provided a fundamental understanding of the SSI issue (Jiang and Yin 2012; Su, Yin, and  
56 Zhou 2010; Zhao, Zhou, and Yuen 2017; Zhou and Yin 2008; Zhou, Yin, and Hong 2011; Zhou,  
57 Yuen, and Tan 2013). Efforts have been made to investigate the influencing factors in the  
58 mechanical behavior of SSI. The laboratory experiments found that the interface roughness affects  
59 the shear resistance and volumetric change of soil shearing at interface (Dejong, White, and  
60 Randolph 2006; Hu and Pu 2005; Paikowsky, Player, and Connors 1995; Su et al. 2018; Uesugi and  
61 Kishida 1986a). In addition, the numerical simulations reveal that the interface roughness is  
62 involved in the stress-strain evolution pattern as well as the strain localization inside soil shearing at  
63 an interface (Frost, Dejong, and Recalde 2002; Jensen et al. 1999; Wang, Gutierrez, and Dove  
64 2007). Furthermore, both the shear resistance and volumetric change of the SSI depend on the soil  
65 properties (Hossain and Yin 2014; Ochiai et al. 1996; J. H. Yin and Zhou 2009). For example, the  
66 initial relative density determines whether the soil dilates or contracts (Dejong, White, and  
67 Randolph 2006; Zhu, Zhou, and Yin 2017), and the shear strength of bulk soil governs the shear  
68 resistance ability at the interface (Hu and Pu 2005; Wang and Jiang 2011).

69 A rich body of investigations has proved that the grain shape emerges as an essential soil property  
70 that affects the various mechanical behaviors of bulk soil. The relationship between the  
71 compactness of the soil and the shape parameter has been exploited in terms of the maximum and  
72 minimum void ratio (Miura et al. 1998; Nakata et al. 2001). The motions of the particles, including  
73 movement and rotation, result in the macroscopic deformation of a granular system. The rotation of  
74 a particle with an irregular shape is restricted and accordingly increases the interlocking inside the  
75 soil, leading to a higher shear strength and a larger dilation (Santamarina and Cho 2004). Moreover,  
76 the shear-induced anisotropy of a granular material composed of non-spherical particles is  
77 emphasized due to the particle eccentricity (Oda, Nemat-Nasser, and Konishi 1985; Rothenburg and  
78 Bathurst 1992). In this context, the particle shape emerges as an essential soil property that needs to



79 be properly considered in the SSI issue. The particle shape is generally characterized using three  
80 scales: roundness, sphericity, and smoothness (Krumbein and Sloss 1951). The sphericity  $S$  is  
81 correlated to the rotation of the particle and the arrangement of the granular material, which are  
82 crucial to the macroscopic behaviors of the granular material. Thus, this study will focus on the  
83 effects of particle sphericity. Furthermore, the orientations of irregular particles will lead to an  
84 initial anisotropy of the specimen (Yin et al. 2010; Chang & Yin 2009). Thus, the effect of initial  
85 fabric on SSI shearing behavior should be discussed as well.

86 The discrete element method (DEM) as a numerical tool has been widely used in the geotechnical  
87 field due to the fact that soil is discontinuous in nature. Two-dimensional (2D) and three-  
88 dimensional (3D) DEM simulations have been successfully applied in the soil-structure interface  
89 issue (Jensen et al. 1999; Frost et al. 2002; Wang & Jiang 2011; Jing et al. 2017b). The particle used  
90 in the early DEM models was a disc in the 2D case and a spherical particle in the 3D case. Certain  
91 methods have been proposed to mimic the behavior of a non-spherical particle in DEM simulation.  
92 For example, the rolling resistant contact law between spherical particles has been proposed to  
93 manually prevent the rotation of particles by introducing a rolling friction coefficient (Ai et al.  
94 2011; Iwashita and Oda 1998; Wensrich and Katterfeld 2012). However, real soil particles are  
95 generally with various shapes, different from idealized granular system with discs and spherical  
96 particles, which significantly affects the mechanical behavior of soils. For this reason, non-spherical  
97 elements have been successfully applied in DEM simulation, such as clustered particles, polygons,  
98 and ellipsoids (Bono and McDowell 2015; Lin and Ng 1997; Lu and McDowell 2007; Ni et al. 2000;  
99 Salot, Gotteland, and Villard 2009). Jensen et al. (1999) employed a clustered element in 2D  
100 simulation of IST. However, how the shear resistance, material fabric, and particle motions are  
101 affected by the particle sphericity and initial fabric during interface shearing has not been fully  
102 studied. Furthermore, the thickness of localized band should be measured under various loading and  
103 modeling conditions.

104 In this study, the effect of particle shape was thoroughly investigated by 3D DEM. Different types  
105 of clustered particles were used to represent the irregular particles with various sphericities.  
106 Specimens were randomly generated and sheared on interfaces with different roughnesses. Based  
107 on the DEM interface shear test results, the following 4 aspects were explored: (1) the effect of  
108 particle sphericity on extreme porosities of granular material, (2) the effect of particle sphericity on  
109 both macro- and micro- shearing behaviors of SSI, (3) the effect of interface roughness on the  
110 behaviors of SSI and (4) the effect of initial fabric on the shearing behaviors of SSI.

## 111 **2. The DEM simulation**

### 112 **2.1 Input parameters**

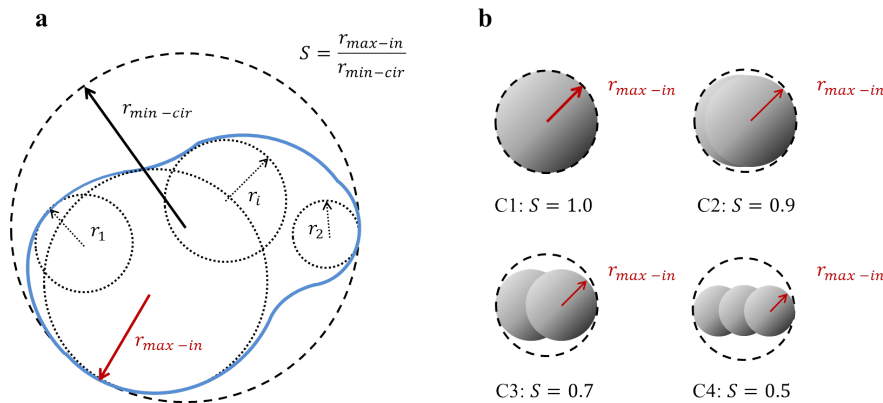
113 PFC 3D 5.0 software based on the discrete element method proposed by (Cundall and Strack 1979)  
114 was employed in this study. The Hertz-Mindlin contact law was used to describe the non-linear  
115 force-displacement relationship between two contacting particles (Mindlin and Deresiewicz 1953).  
116 The shear modulus  $G$  and Poisson's ratio  $\nu$  were used to describe the deformability of the granular  
117 material. The values of the input parameters used in this study refer to the 3D simulation performed  
118 by Lin and Ng (1997) using arrays of ellipsoids, in which the shear modulus  $G$  was 28.957 GPa, the  
119 Poisson's ratio  $\nu$  was 0.15 and the inter-particle friction coefficient  $\mu_p$  was 0.5. A damping  
120 coefficient with a value of 0.7 was applied to dissipate the energy together with the sliding and  
121 guarantee a quasistatic analysis.

### 122 **2.2 Geometries of the clumps**

123 A clustered particle, named clump, can be formed by adding certain particles together with or  
124 without overlapping. Efforts were made to bring the geometry of the clump close to that of real sand  
125 grain by composing more particles with the help of a 3D scanning technique or specific algorithms.  
126 Those sophisticated approaches validated the significance of the particle shape in the DEM

127 simulation but created another problem. It was time-consuming, because of the remarkably  
 128 increased particle numbers, to form a clustered element that would be closer to the real one. It has  
 129 been asserted that a clump having asymmetry geometry is sufficiently close to the mechanical  
 130 behavior of real soil material. Thus, clumps composed of two or three single particles were enough  
 131 for the simulation, which took into account the effect of particle shape (Coetzee 2016; Salot,  
 132 Gotteland, and Villard 2009).

133 The sphericity  $S$  is characterized as shown in Fig. 1a (Krumbein and Sloss 1951). The  $r_{max\_in}$  is  
 134 the radius of the maximum inscribed sphere, and the  $r_{min\_cir}$  is the radius of the minimum  
 135 circumscribed sphere of the irregular particle. The clumps, composed of different numbers of  
 136 spherical particles representing various sphericity  $S$  used in the model, are named C1, C2, C3, and  
 137 C4, respectively (Fig. 1b).



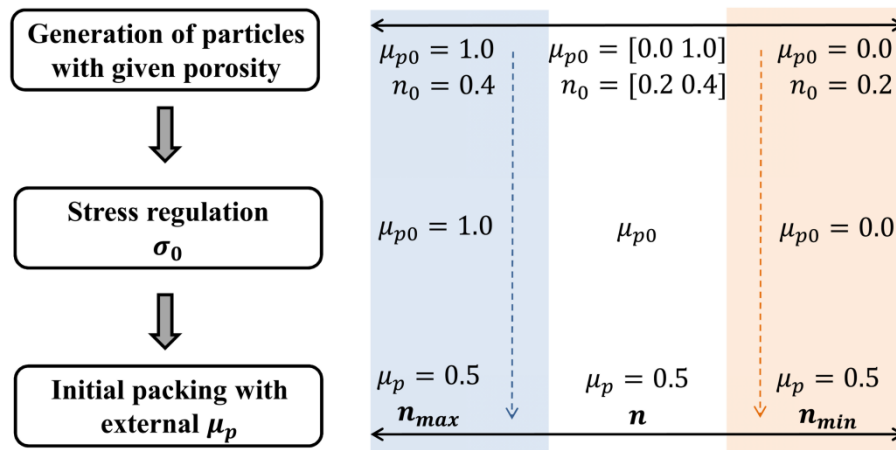
138

139 Fig. 1. (a) Definition of the sphericity  $S$  (Krumbein and Sloss 1951); (b) clumps used in this study

### 140 2.3 Specimen generation process

141 The specimen preparation method refers to the procedure proposed by Muir and Kenichi (2007) to  
 142 obtain a granular material with varied porosity  $n$  (Fig. 2). The specimen followed a given particle-  
 143 size distribution, and a specific initial porosity  $n_0$  was randomly generated inside a container with  
 144 six frictionless walls. To obtain the densest granular material, the initial friction coefficient between

145 particles  $\mu_{p0}$  was set to zero and the initial porosity  $n_0$  of the specimen was set to 0.2. Overlapping  
 146 particles immediately spread out or separated to achieve an equilibrium state. Then the walls of the  
 147 container were controlled by a servo system until the mean stress on the walls reached a given value  
 148  $\sigma_0$  by moving slowly inward or outward. The friction coefficient of particle  $\mu_{p0}$  changed to the  
 149 eventual value  $\mu_p$  and was maintained as a constant in the shearing stage. Then the final porosity of  
 150 the specimen regained the equilibrium state, which was defined as the minimum porosity  $n_{min}$ . In  
 151 contrast, to obtain a “loosest” specimen, the initial friction coefficient of particle  $\mu_{p0}$  was set to 1.0  
 152 to generate a specimen with a high  $n_0$  equals 0.4. Then the same procedure was performed to obtain  
 153 the loosest sample. The eventual porosity  $n$  of the granular material can be altered by inputting a  
 154 different value of  $\mu_{p0}$  and  $n_0$ .



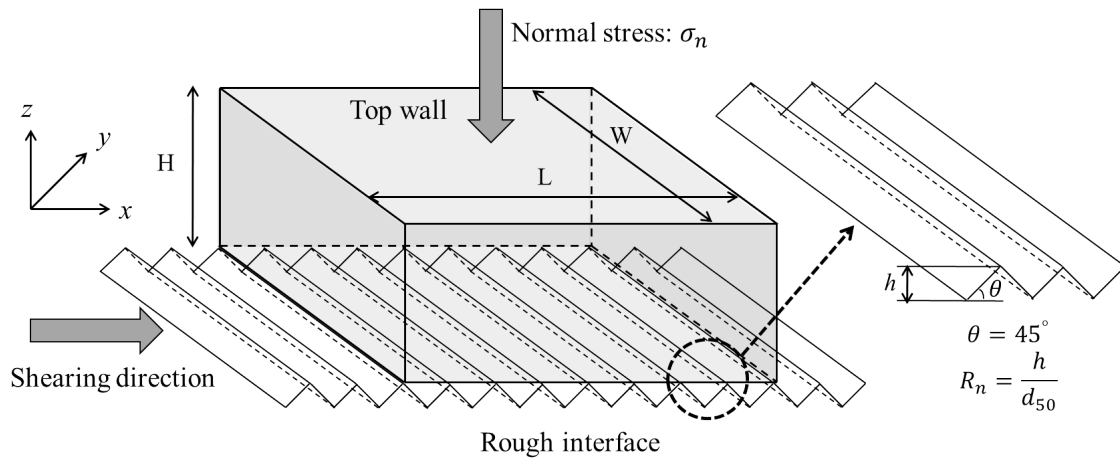
155  
 156 Fig. 2. Specimen generation procedure after Muir and Kenichi (2007)

157 **2.4 The simulation of soil-rough interface shearing**

158 The numerical model of soil-rough interface shear test is illustrated in Fig. 3. The dimension of the  
 159 shear box is described using length (L), width (W), and height (H). A regular saw-tooth wall is used  
 160 in the model with an inclined angle  $\theta$  equals  $45^\circ$  and a depth of each valley  $h$ . The normalized  
 161 roughness  $R_n$  of this continuum interface is defined as  $h/d_{50}$  referring to the definition proposed by

162 Uesugi and Kishida (1986b), where  $d_{50}$  is the mean particle diameter. The value of  $R_n$  is 0.5 in the  
 163 following simulations. Four specimens consisting of clumps C1, C2, C3, and C4, respectively, have  
 164 been generated with a desired porosity  $n$ . Equivalent diameter  $d_{eq}$  is denoted for the clumps with a  
 165 non-spherical shape, which is defined as the diameter of a spherical ball with the same volume as  
 166 the clump. All specimens follow a same linear grain size distribution. The value of  $d_{eq}$  ranges  
 167 between 1.8 mm and 3.6 mm, and the  $d_{50(eq)}$  equals 2.7 mm.

168 Once the granular material reached an equilibrium state, a constant normal stress  $\sigma_n$  was applied on  
 169 the top wall. The bottom rough interface wall began to move horizontally in  $x$ -direction at a low  
 170 speed once the granular system was stabilized. The four lateral walls were fixed, and the top wall  
 171 was vertically moveable during the shearing loading process. The top wall was controlled by a  
 172 servo system to maintain a constant normal stress.



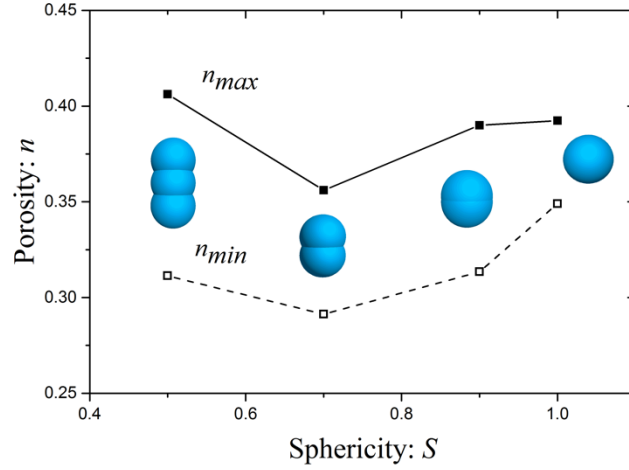
174 Fig. 3. Schematic diagram of interface shear test in the DEM simulation

175 The macroscopic mechanical behaviors were measured according to the displacements and forces of  
 176 the walls. The shear stress  $\tau$  was the shear force measured on the interface wall divided by the area  
 177 of horizontal section of the shear box. The shear displacement  $d_s$  was the displacement of the  
 178 bottom wall in the direction of shearing. The normal stress  $\sigma_n$  was measured on the top wall. The

179 vertical displacement  $d_v$  of the top wall was recorded to reflect the volumetric change of the  
180 specimen.

### 181 **3. The compactness of the specimen**

182 In this study, the maximum porosity  $n_{max}$  and minimal porosity  $n_{min}$  of a specimen composed of  
183 different clumps were obtained using the procedure introduced in section 2.3. The values of  $n_{max}$   
184 and  $n_{min}$  of various specimens are illustrated in Fig. 4, which shows that the specimen composed of  
185 spherical particles ( $S = 1.0$ ) tends to form a loose configuration. Non-spherical particles allow a  
186 better filling of the void space compared to spherical particles, and as a result, a dense packing is  
187 achieved for the specimen with a smaller value of  $S$ . On the other hand, rolling easily occurs with  
188 spherical particles ( $S = 1.0$ ) and leads to a similar configuration of the granular assembly at the  
189 loosest and densest configurations. Accordingly, the difference between the  $n_{max}$  and  $n_{min}$  for the  
190 specimen with spherical particles ( $S = 1.0$ ) is smaller than the others with irregular particles. It  
191 should be noted that the most elongated clump ( $S = 0.5$ ) can form a structure with more void space  
192 and correspondingly results in a higher value of  $n_{max}$ . As mentioned by Salot et al. (2009), the  
193 extreme porosities obtained in the numerical simulation cannot compare directly with those  
194 obtained in the experimental tests because of the difference in preparation procedure. However, it is  
195 necessary to control the relative density of the granular material when taking into account the  
196 particle shape effect in the DEM tests.



197

198 Fig. 4. The extreme porosities  $n_{max}$  and  $n_{min}$  of the specimen featuring various sphericity  $S$

199 **4. Effect of particle shape and interface roughness**

200 The relative density  $D_r$  of the granular material is calculated by  $D_r = \frac{(n_{max}-n)(1-n_{min})}{(n_{max}-n_{min})(1-n)}$

201 (

202 1

203 
$$D_r = \frac{(n_{max}-n)(1-n_{min})}{(n_{max}-n_{min})(1-n)} \quad (1)$$

205 b Four specimens consisting of spheres and three types of clumps were generated, named S1, S2, S3,

206 e and S4, respectively. Each specimen comprised around 30,000 spheres or clumps. The dense

207 l configuration was guaranteed by controlling the  $D_r = 90\%$  for all specimens. The desired initial

208 o porosities  $n_0$  of each specimen were derived according to  $D_r = \frac{(n_{max}-n)(1-n_{min})}{(n_{max}-n_{min})(1-n)}$

209 w

255 (1 as listed in Table 1. To demonstrate the effect of particle sphericity on the macroscopic

210 , mechanical behavior of the SSI, sixty ISTs of specimen S1/2/3/4 shear on a rough interface

257 featuring  $R_n = 0.1/0.25/0.5/0.75/1.0$  under a normal stress  $\sigma_n$  equals 25 MPa/50 MPa/100 MPa

258 R respectively were modeled. The generation procedure is presented in section 2.3.

214 E

215 F

217 \_

218 R

259 Table 1. Summary of the numerical tests with various elements

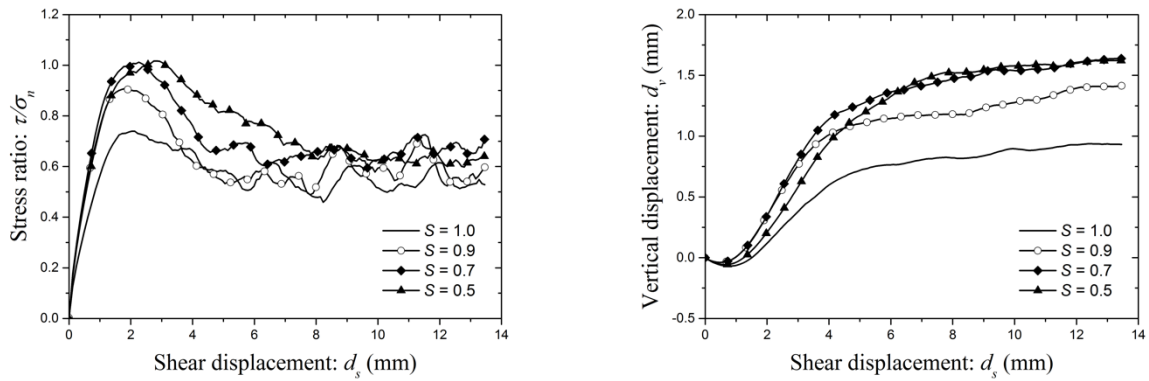
Specimen	Sphericity	Normalized roughness of interface: $R_n$	Initial porosity: $n_0$
S1	$S = 1.0$	0.1	0.359
		0.25	0.353
		0.5	0.355
		0.75	0.352
		1.0	0.357
S2	$S = 0.9$	0.1	0.325
		0.25	0.329
		0.5	0.326
		0.75	0.322
		1.0	0.321
S3	$S = 0.7$	0.1	0.306
		0.25	0.309
		0.5	0.301
		0.75	0.297
		1.0	0.297
S4	$S = 0.5$	0.1	0.323
		0.25	0.326
		0.5	0.323
		0.75	0.325
		1.0	0.325

260 **4.1 Macroscopic response**

261 The macroscopic mechanical behaviors of the ISTs comprising particles of various  $S$  are illustrated  
262 in Fig. 5 in terms of the stress ratio  $\tau/\sigma_n$  and the vertical displacement  $d_v$  as a function of shear  
263 displacement  $d_s$ . As shown in Fig. 5a, the evolutions of  $\tau/\sigma_n$  of the four tests display a similar  
264 tendency. Stress softening occurs once the  $\tau/\sigma_n$  peaks. Note that the peak shear stress at the  
265 interface is affected by particle sphericity  $S$ . The specimens composed of non-spherical particles  
266 show a higher peak shear stress than one composed of spherical balls ( $S = 1.0$ ). The difference in



267 shear resistance is attributed to the interlocking phenomenon between the particles. Unlike the way  
 268 a spherical particle easily rotates when making contact with another one, an irregular particle tends  
 269 to interlock with other particles or the rough interface. The evolution of vertical displacement of the  
 270 top wall  $d_v$  reflects the volumetric change in the specimen, showing that all specimens contract at  
 271 the beginning of shearing and then gradually dilate. The growing rate of dilation slows down at  
 272 shear displacement  $d_s$  where shear stress softening appears. This suggests that the volumetric  
 273 change in the specimen is also affected by the particle sphericity. A larger dilatancy can be  
 274 observed in the specimen with non-spherical particles. From the perspective of micro-mechanics,  
 275 the volumetric change of a granular material is the result of the micro-physics of individual  
 276 particles, i.e., movement and rotation. To help explain the macroscopic responses we obtained in  
 277 the simulations, the micro-physics of the particles will be analyzed in the following sections.



278

(a)

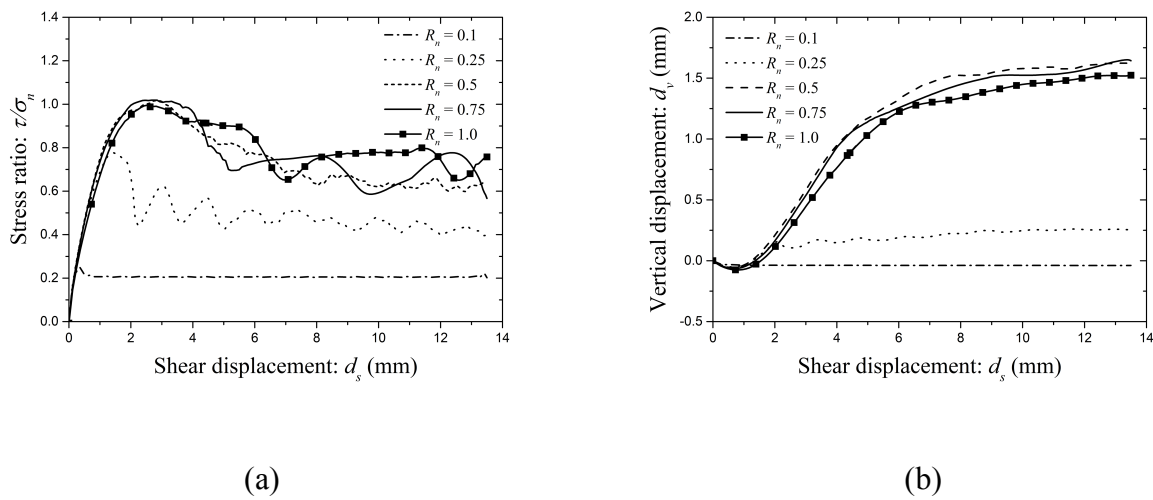
(b)

279

280 Fig. 5. Macroscopic responses of the ISTs comprising particles of various  $S$  ( $D_r = 90\%$ ,  $R_n = 0.5$ ,  
 281  $\sigma_n = 50$  MPa): (a) stress ratio  $\tau/\sigma_n$  versus shear displacement  $d_s$ ; (b) vertical displacement  $d_v$   
 282 versus shear displacement  $d_s$

283 The macroscopic mechanical behaviors of the ISTs ( $S = 0.5$ ) featuring varying  $R_n$  under  $\sigma_n = 50$   
 284 MPa are illustrated in Fig. 6. As shown in the figure, the peak shear stress ratio and volumetric  
 285 change are affected by the  $R_n$ . A higher peak shear stress and larger dilation are observed when the

286 specimen shearing on a rougher interface. This result is consistent with the existing experimental  
 287 findings (Hu & Pu, 2005; Paikowsky et al., 1995), the shear strength of interface generally increases  
 288 as the increasing of  $R_n$ . Note that periodic oscillation is observed in the curve of  $\tau/\sigma_n$  when  $R_n =$   
 289 0.25. In this case, the clumps in the bottom layer cannot fit into such small volumes between  
 290 sawteeth. Thus, the bottom layer of clumps moves alternately between the tops of the teeth and the  
 291 areas between teeth, which results in periodic oscillation in the total contact number between the  
 292 bottom clumps and interface. This induces this kind of evolution of  $\tau/\sigma_n$ .



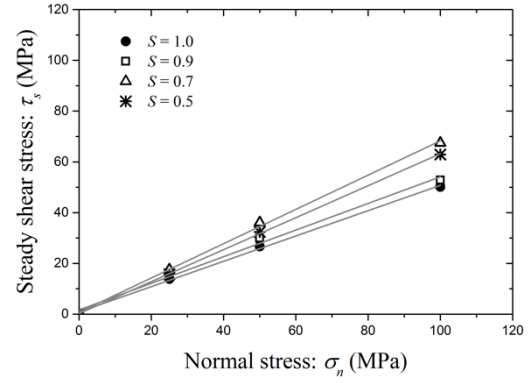
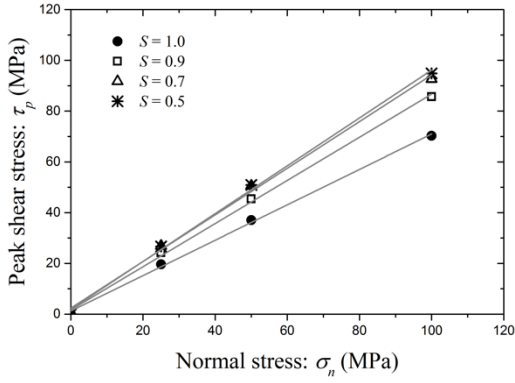
293

294

295 Fig. 6. Macroscopic responses of the ISTs ( $S = 0.5$ ,  $\sigma_n = 50$  MPa) featuring varying normalized  
 296 roughness  $R_n$ : (a) stress ratio  $\tau/\sigma_n$  versus shear displacement  $d_s$ ; (b) vertical displacement  $d_v$   
 297 versus shear displacement  $d_s$

#### 298 4.2 Interface friction angle analysis

299 The peak shear stress  $\tau_p$  and steady shear stress  $\tau_s$  (at  $d_s = 13.5$  mm) were obtained for the ISTs  
 300 under various normal stress 25 MPa/50 MPa/100 MPa. According to the Mohr-Coulomb criterion,  
 301 the peak friction angle  $\phi_p$  and steady friction angle  $\phi_s$  can be obtained by linearly fitting the  $\tau_p$  and  
 302  $\tau_s$  under various normal stress conditions (Fig. 7a/7b). The cohesive force was assumed to be zero  
 303 since a non-cohesive soil was considered in this study.



304

305

306

307

308

309

310

311

312

313

(a)

(b)

Fig. 7. (a) Fitting the peak shear stress  $\tau_p$  as a function of normal stress  $\sigma_n$ ; (b) fitting the steady shear stress  $\tau_s$  as a function of normal stress  $\sigma_n$  ( $R_n = 0.5$ )

The friction angles of all ISTs are obtained by this criterion to discuss the effects of  $S$  and  $R_n$  on the shear resistance of SSI. As a reference, the direct shear tests (DSTs) with the same input parameters under  $\sigma_n$  equals 25 MPa/50 MPa/100 MPa are modeled. The height of the interface shear box is twice of the specimen in IST. The peak friction angles of ISTs ( $\phi_p$ ) and DSTs ( $\phi_p^d$ ) are summarized in Table 2.

Table 2. Summary of the peak friction angles of ISTs and DSTs

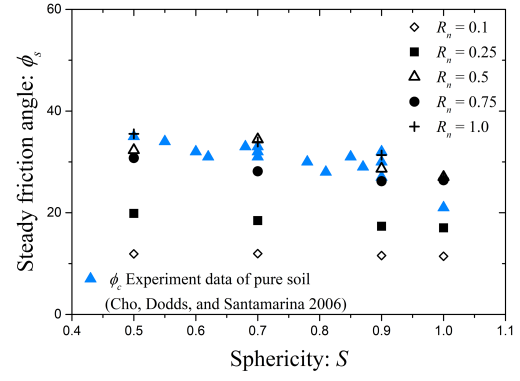
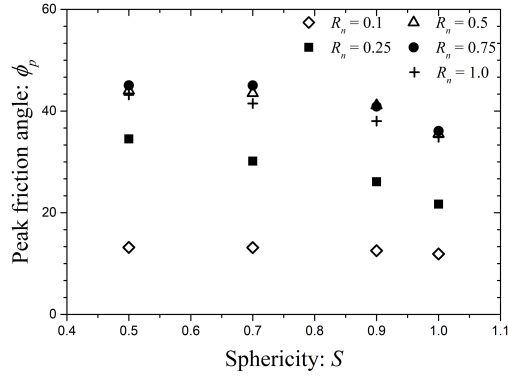
Sphericity	Peak friction angle (°)					DST
	$R_n = 0.1$	$R_n = 0.25$	$R_n = 0.5$	$R_n = 0.75$	$R_n = 1.0$	
$S = 1.0$	11.89	21.70	35.51	36.07	34.85	35.74
$S = 0.9$	12.54	26.10	41.10	40.89	38.02	43.84
$S = 0.7$	13.14	30.15	43.53	45.05	41.48	49.42
$S = 0.5$	13.18	34.53	44.05	45.06	43.19	47.30

314

#### 315 4.2.1 Effect of sphericity

316 The peak friction angles  $\phi_p$  and steady friction angles  $\phi_s$  measured in all ISTs are plotted in Fig. 8.  
317 Existing research studies reveal that the interface shear strength is profoundly correlated with the  
318 shear strength of pure soil. The friction angle measured on a rough IST is close to the friction angle  
319 of pure soil (Chen et al. 2015; Frost, Dejong, and Recalde 2002; Jing et al. 2017; Rao, Allam, and  
320 Robinson 1998; Uesugi, Kishida, and Tsubakihara 1988). For this reason, the steady friction angles  
321  $\phi_s$  obtained in the numerical ISTs are compared to the critical friction angles  $\phi_c$  of pure soil  
322 obtained in the laboratory experiments in Fig. 8b. The experimental databases are derived from the  
323 study of Cho, Dodds, and Santamarina (2006). The tested soils include crushed sands and natural  
324 sands from various places, and some other materials such as glass beads and granite powder.

325 Fig. 8a shows that the value of  $\phi_p$  increases with the decreasing of the sphericity  $S$  when  $R_n \geq$   
326 0.25. It implies that the shear strength of SSI is enhanced by the interlocking between interface and  
327 particles. This augment due to the particle irregularity is not evident when the specimen shearing on  
328 a relative smooth interface ( $R_n = 0.25$ ). Because in this case, the shear strength at SSI primarily  
329 originates from the friction between soil particles and interface. Note that the  $\phi_s$  shows a similar  
330 trend for  $\phi_p$  except when  $S$  equals 0.7 in the case  $R_n = 0.5$ , in which the  $\phi_s$  is lower than the one  
331 where  $S$  equals 0.7. This might be explained by the way the shear stress is not perfectly constant but  
332 varies slightly at the steady shear stress state. Moreover, the interaction between two elongated  
333 particles ( $S = 0.5/0.7$ ) and the saw-tooth surface is similar, inducing approximate friction angles for  
334 the two cases. The evolution trend of  $\phi_s$  at various  $S$  is similar to that of the  $\phi_c$  obtained in the  
335 laboratory experiment. This result verifies the accuracy of the numerical simulation to a certain  
336 degree. It suggests a correlation between the particle sphericity and the friction angle of SSI in the  
337 case of relative rough interface.



(a)

(b)

338

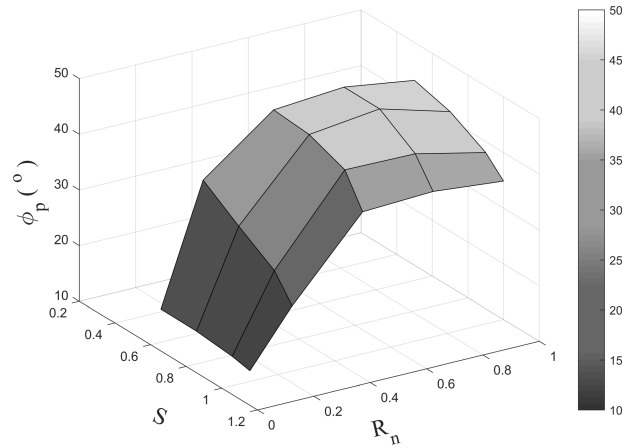
339

340 Fig. 8. (a) Peak friction angle  $\phi_p$  obtained in the DEM ISTs; (b) comparison of the steady friction  
 341 angle  $\phi_s$  obtained in the DEM ISTs to the critical friction angle  $\phi_c$  of pure soil obtained in the  
 342 laboratory experiments (Cho, Dodds, and Santamarina 2006) at varying sphericity  $S$

#### 343 4.2.2 Effect of interface roughness $R_n$

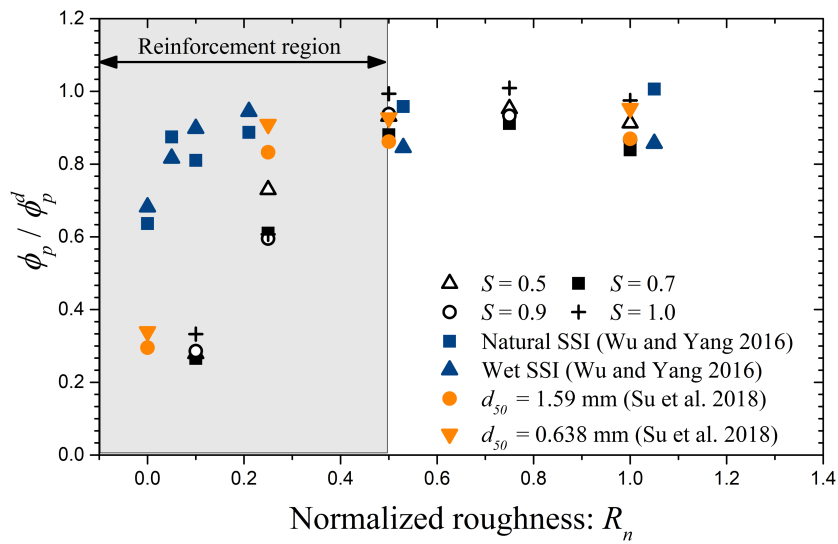
344 The peak friction angle  $\phi_p$  measured on SSI is affected by  $R_n$  as well as  $S$  as illustrated in Fig. 9. In  
 345 general, the value of  $\phi_p$  increases as the increasing of  $R_n$ . This tendency is valid for the specimens  
 346 featuring varying sphericity  $S$ . To compare the numerical results to the laboratory experiment  
 347 results, the friction angles  $\phi_p$  measured in IST is normalized by the  $\phi_p^d$  obtained in DST. The ratios  
 348 of  $\phi_p/\phi_p^d$  at varying  $R_n$  are plotted in Fig. 10. The experimental data are derived from the ISTs  
 349 between natural soil and steel plate (Su et al. 2018; Wu and Yang 2016). Fig. 10 illustrates that the  
 350 value of  $\phi_p/\phi_p^d$  increases significantly in the range of  $R_n$  between 0 and 0.5. The growing rates of  
 351 these tests are different, which depend on the properties of soil material, e.g. friction, grading, water  
 352 content, particle size, particle shape and etc. When the value of  $R_n$  is greater than 0.5, the ratios of  
 353  $\phi_p/\phi_p^d$  achieve to a plateau value. It implies that the interaction between particles and interface  
 354 similar to the interaction among pure particles when  $\phi_p/\phi_p^d$  is close to 1.0. Note that the  $\phi_p/\phi_p^d$  of  
 355 the IST of  $R_n = 1.0$  are slightly less than those of  $R_n = 0.5$  and 0.75 in the numerical tests. In this  
 356 case, the bottom particles of approximately uniform distributed sample ( $C_n \approx 1.45$ ) will be trapped

357 in the valley between sawteeth of interface, which weakens the interlocking between particles and  
 358 interface. In contrast, for the well graded soil sample ( $C_n = 19.2$ ) used by Wu and Yang (2016), the  
 359 soil particles can properly fit in the space of rough interface, leading to a stronger interlocking.



360

361 Fig. 9. The peak friction angle  $\phi_p$  at varying normalized roughness of interface  $R_n$  and sphericity  $S$

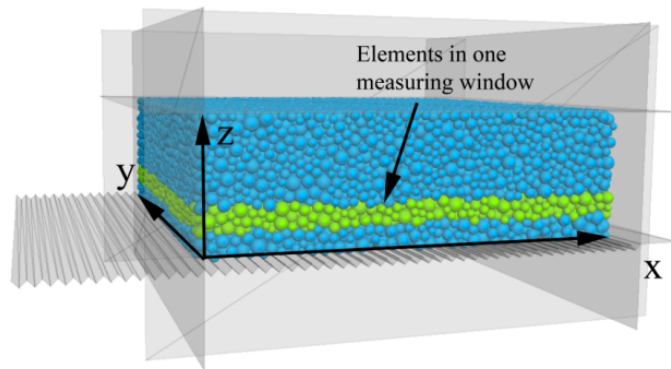


362

363 Fig. 10. Comparison of the friction angle ratio  $\phi_p/\phi_p^d$  obtained in the DEM to those measured in  
364 the laboratory experiments (Su et al. 2018; Wu and Yang 2016) at varying normalized roughness  
365  $R_n$  of interface

### 366 4.3 Localized band analysis

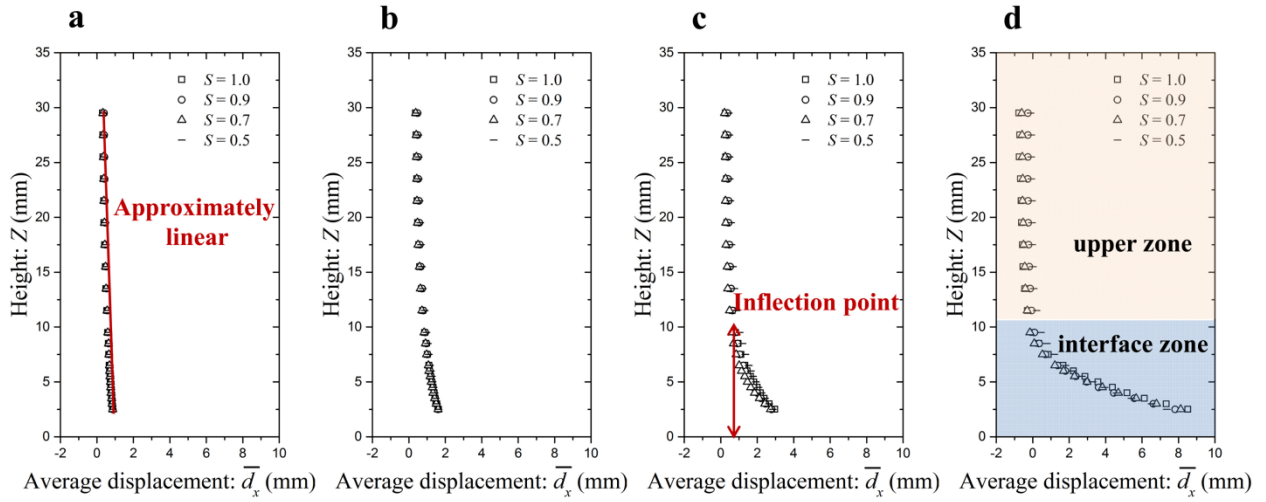
367 Shearing deformation is largely localized in a narrow zone during the shearing process, named the  
368 localized band. The localized band can be analyzed by tracing the movements of each particle at a  
369 specific stress state. To average the kinematic field, we set certain measuring windows at different  
370 heights for the specimen with a dimension of 100 mm  $\times$  100 mm  $\times$  5 mm (Fig. 11). The average  
371 shear displacement in  $x$ -direction  $\bar{d}_x$  of the elements in each measuring window is calculated.



372  
373 Fig. 11. Set-up of measuring window at different heights  $Z$  of the specimen

374 The values of  $\bar{d}_x$  as a function of  $Z$  at different shear stress states ( $R_n = 0.5$ ,  $\sigma_n = 50$  MPa) are  
375 plotted in Fig. 12. Each dot in the figure represents one measurement at a specific height  $Z$ . As the  
376 shear stress increases,  $\bar{d}_x(Z)$  shows a non-linearity, and an inflection point appears. The  
377 phenomenon of stratification becomes more evident at the steady stress state. The shear  
378 displacement induced by the interface shearing largely concentrates in the bottom layer of particles  
379 adjacent to the interface, named the localized band, rather than in the upper zone separate from the  
380 interface. It is consistent with the numerical result regarding the formation of the localized band in

381 2D/3D DEM simulations (Wang et al. 2007; Jing et al. 2017a) as well as the laboratory experiments  
 382 using image analysis (Hu and Pu 2005).



383  
 384 Fig. 12. Average shear displacement in  $x$ -direction  $\bar{d}_x$  of four ISTs ( $R_n = 0.5$ ,  $\sigma_n = 50$  MPa) at  
 385 different shear states: (a)  $d_s = 1.0$  mm; (b)  $d_s = 2.0$  mm; (c)  $d_s = 4.0$  mm; and (d)  $d_s = 13.5$  mm

386 The inflection point of the curve of  $\bar{d}_x(Z)$  at the steady stress state (when  $d_s/d_{50} = 3.5$ ) is used to  
 387 define the thickness of the localized band  $\delta_h$ . Spline interpolation is applied to get a smooth  $\bar{d}_x - Z$   
 388 curve  $f(Z)$ . The first derivative  $f'(Z)$  and second derivative  $f''(Z)$  are calculated using the finite  
 389 difference method. The curvature  $\kappa$  of  $f(Z)$  is defined by Eq. 2,

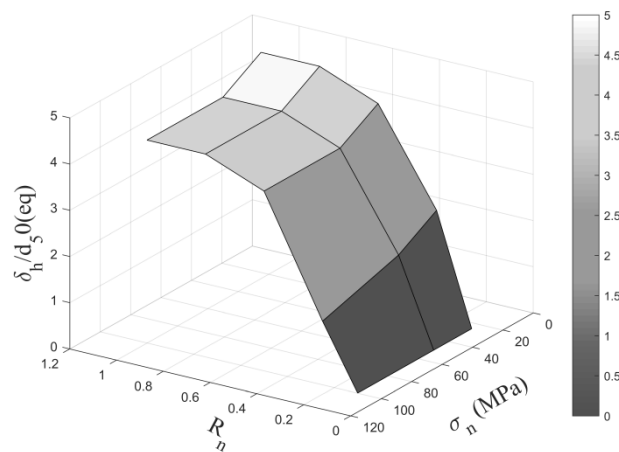
390

$$\kappa = \frac{|f''(Z)|}{(1 + f'(Z)^2)^{3/2}} \quad (2)$$

391 The  $\bar{d}_x$  changes approximately linearly with the height  $Z$  toward the higher position of the specimen  
 392 where the value of  $\kappa$  approaches zero. As  $Z$  decreases, the  $\kappa$  sharply increases at a certain value of  $Z$   
 393 because of the localization of shear deformation. Thus, the inflection point of the  $\kappa$  is considered as  
 394 a sign of the top boundary of the localized band. Jing et al. (2017a) suggest that the inflection point  
 395 is where the  $\kappa$  equals 0.02.



396 According to this criterion, the thicknesses of the localized band  $\delta_h$  is rarely affected by the particle  
 397 sphericity  $S$  (Fig. 12). However, Fig. 13 shows that  $\delta_h$  is affected by  $R_n$  and  $\sigma_n$  and it ranges  
 398 between 0 and 5 times of  $d_{50(eq)}$ . The localized band is structuralized inside the material when it  
 399 shearing on a relative rough interface. A thicker localized band is observed in the IST featuring a  
 400 rougher interface, which suggests that the failure shifts from the interface into the soil layer. The  
 401 specimen subjected to a lower normal stress condition ( $\sigma_n = 25$  MPa) tends to form a thicker  
 402 localized band because the material dilates more under a lower confining stress.



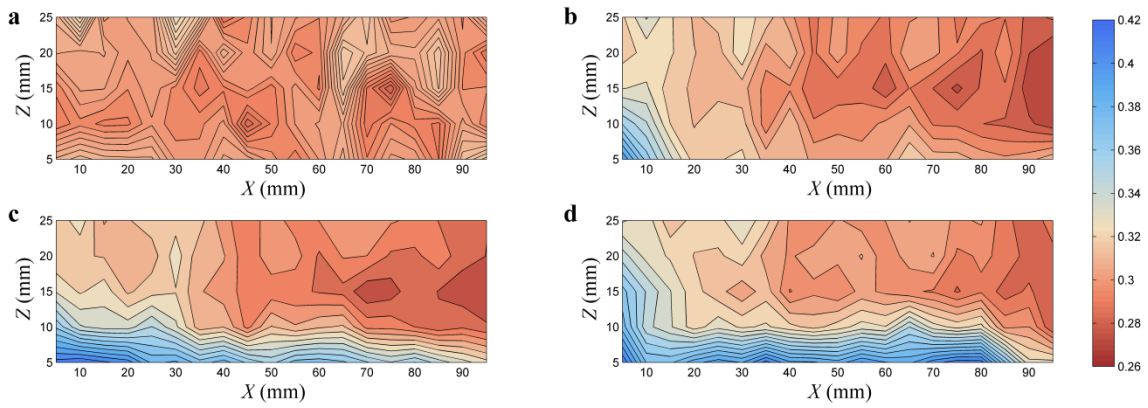
403

404 Fig. 13. Normalized thicknesses of localized band  $\delta_h/d_{50(eq)}$  of ISTs ( $S = 0.5$ ) at different normal  
 405 stress  $\sigma_n$  and interface roughness  $R_n$

#### 406 4.4 Local porosity and coordination number

407 To help visualize the local porosity distribution inside the specimen, a grid is constructed to  
 408 compute the contour of local porosity. Certain measuring balls are set inside the shear box. All the  
 409 centers of measuring balls are located in the central cross-section of shear box, which represent the  
 410 nodes of the grid. The porosity obtained in each measuring ball represents the local porosity at the  
 411 position of the center of ball, in another word, the node of grid. Accordingly, the contour of local  
 412 porosity can be obtained. The contours of local porosity for the IST ( $S = 0.7$ ) at different strain  
 413 states are plotted in Fig. 14, showing that the initial distribution of porosity is almost homogenous.

414 As shearing progresses, the particles gradually accumulate on the right side and accordingly lead to  
 415 the dilation on the bottom left corner of the specimen. The dilation region enlarges from the bottom  
 416 left corner to the bottom part of the entire specimen. The difference in the local porosity inside the  
 417 specimen reaffirms that the granular material is structuralized into two regions when shearing on an  
 418 interface (section 4.3). The top line of the localized region is not strictly horizontally straight  
 419 because of the fixed lateral walls that prevent the movement trend of particles.



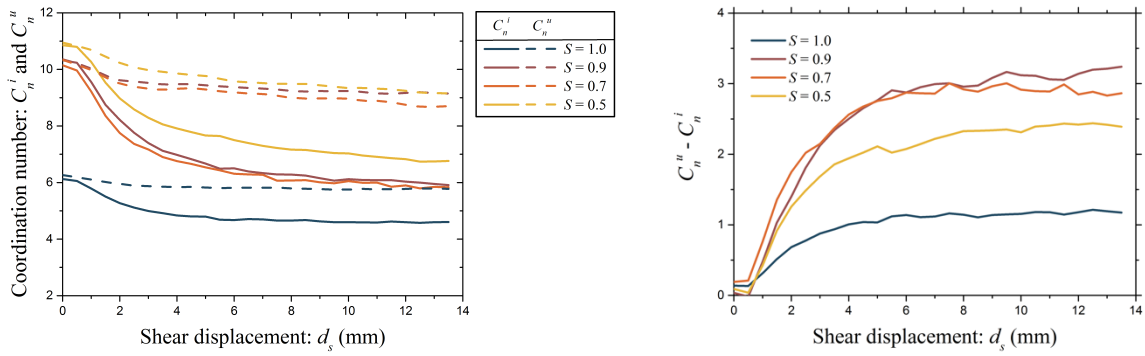
420  
 421 Fig. 14. Local porosity inside the central section of the specimen ( $R_n = 0.5, S = 0.7$ ) at different  
 422 strain states: (a)  $d_s = 0.0$  mm; (b)  $d_s = 2.0$  mm; (c)  $d_s = 4.0$  mm; and (d)  $d_s = 13.5$  mm

423 The coordination number  $C_n$  is used to describe the local contact at particle scale, which is  
 424 profoundly correlated to the porosity of the granular assembly. It is defined as the average contact  
 425 number per particle (Eq. 3),

426 
$$C_n = (\sum_{N_p} n_c^p) / N_p \quad (3)$$

427 where  $N_p$  is the total number of particles in the measured region, and  $n_c^p$  is the contact number of  
 428 particles  $p$  in the measured region. As discussed in section 4.3, the specimen structuralizes into two  
 429 regions after shearing, the interface zone and upper zone (Fig. 12d). The evolutions of the  
 430 coordination number inside the interface zone  $C_n^i$  and the upper zone  $C_n^u$  for the ISTs with various  $S$   
 431 are illustrated in Fig. 15a. The initial coordination number of the specimen composed of irregular

432 clumps is much higher than the one consisting of spherical balls, which suggests that more contacts  
 433 exist between the irregular particles. It explains why interlocking tends to occur inside such  
 434 granular material. A sharp decrease for  $C_n^i$  is observed in all cases; in contrast, the change in  $C_n^u$  is  
 435 minor. The dilation primarily occurs in the interface zone as the contour of local porosity illustrates.  
 436 The micro-structure of particles in the upper zone is almost preserved. Fig. 15b shows the  
 437 difference between the values measured in the interface zone and upper zone  $C_n^u - C_n^i$ . The values  
 438 of  $C_n^u - C_n^i$  increase gradually and approach a steady value. Note that the value in the case of  
 439 spherical balls is much smaller than the others, in which the total volumetric change is the smallest.



440

441 Fig. 15. (a) Coordination number inside the interface zone  $C_n^i$  and upper zone  $C_n^u$  of the ISTs ( $R_n =$   
 442  $0.5, \sigma_n = 50$  MPa) with varying sphericity  $S$ ; (b) the difference between the value measured in  
 443 interface zone and upper zone  $C_n^u - C_n^i$

#### 444 4.5 Material fabric analysis

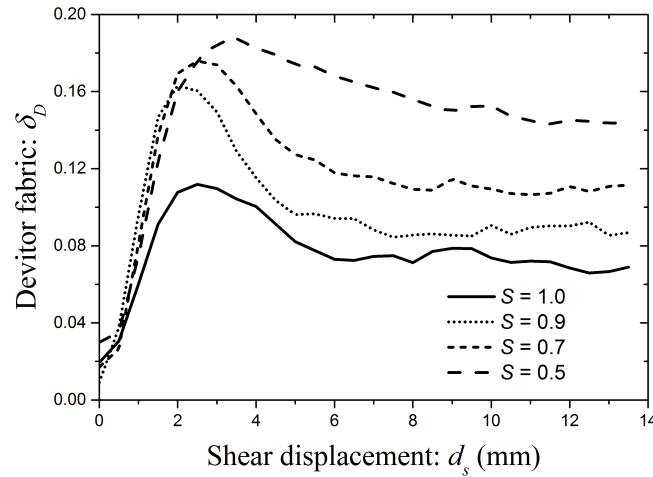
445 The macroscopic mechanical behavior of the granular material originates in the distribution and  
 446 evolution of the material fabric. The distribution of the contact orientation is frequently used to  
 447 describe the material fabric. A second-order tensor  $F_{ij}$  introduced by Satake (1982) is used to  
 448 quantitatively characterize the distribution in normal contact orientation:

$$449 F_{ij} = \frac{1}{N_c} \sum_{\alpha}^{N_c} n_i^{\alpha} n_j^{\alpha} \quad (i, j = x, y, z) \quad (4)$$

450 where  $N_c$  is the total contact number, and  $n_i$  is the contact normal vector at contact  $\alpha$ . The principal  
 451 values of  $F_{ij}$ , ordered by decreasing magnitude, are  $F_1$ ,  $F_2$ , and  $F_3$ . To measure the anisotropy of the  
 452 material fabric, a deviator fabric  $\delta_D$  of  $F_{ij}$  is calculated as follows (Barreto, O'Sullivan, and  
 453 Zdravkovic 2009):

$$454 \quad \delta_D = \frac{1}{\sqrt{2}} [(F_1 - F_2)^2 + (F_2 - F_3)^2 + (F_1 - F_3)^2]^{0.5} \quad (5)$$

455 The evolution of  $\delta_D$  measured in the interface zone for the ISTs under  $\sigma_n = 50$  MPa is plotted in  
 456 Fig. 16. The initial values of  $\delta_D$  are slightly higher than zero because anisotropy is induced by the  
 457 one-dimensional normal pressure before shearing. The  $\delta_D$  increases with the increasing of shear  
 458 displacement  $d_s$  and decreases once the stress softening appears. The peak value of  $\delta_D$  depends on  
 459 particle sphericity. The clumps with smaller sphericity  $S$  induce higher anisotropy during the  
 460 interface shearing, in which a higher interface shear strength is measured. This implies that a  
 461 correlation exists between  $\delta_D$  and interface shear strength.



462

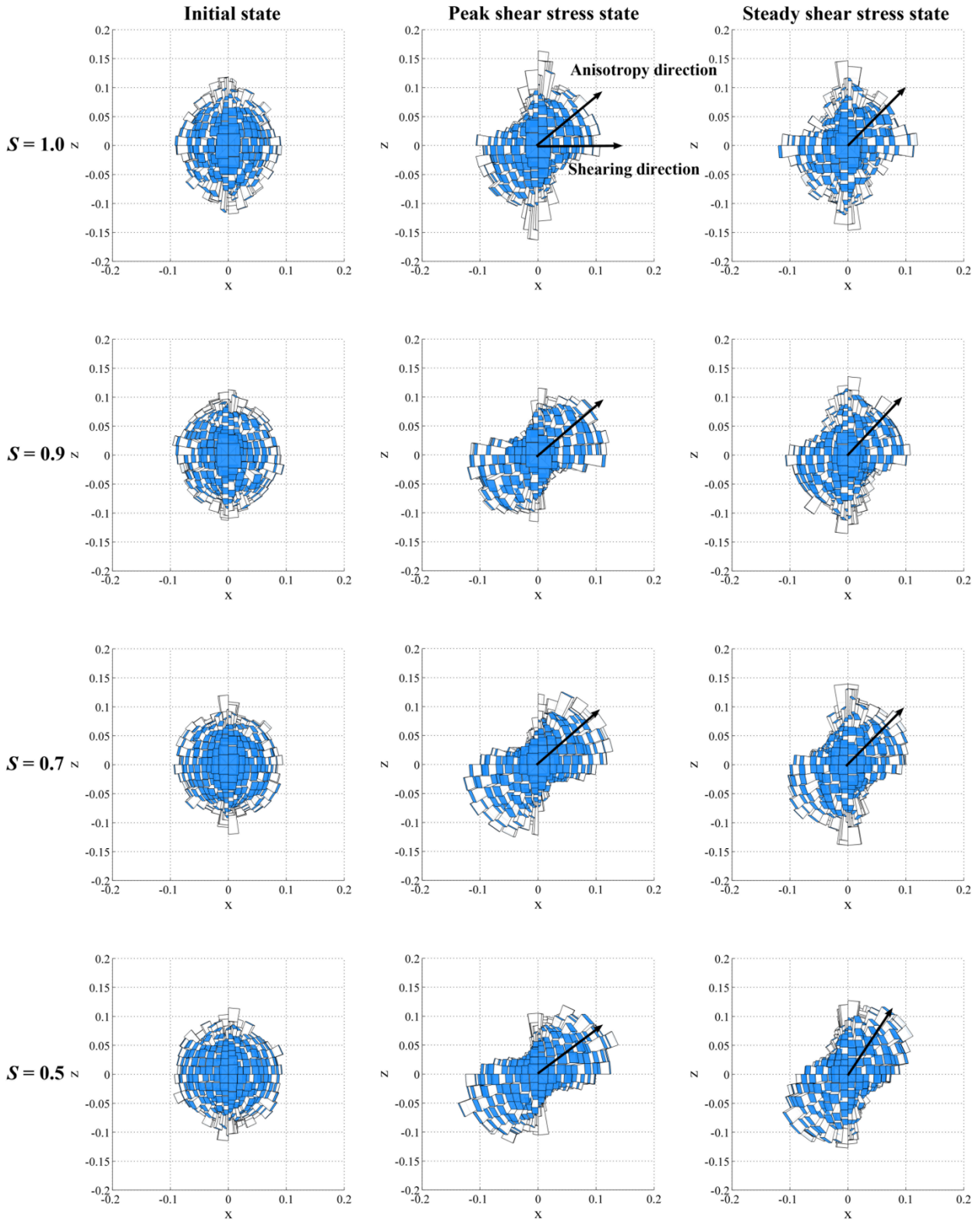
463 Fig. 16. The evolution of deviator fabric  $\delta_D$  in the interface zone of the ISTs with various  
464 sphericities  $S = 1.0/0.9/0.7/0.5$  ( $\sigma_n = 50$  MPa,  $R_n = 0.5$ )

465 The probability density distribution  $P(\vec{n})$  of a unit vector of contact normal  $\vec{n}$  is characterized to  
466 better visualize the contact distribution inside a granular material. The unit vector  $\vec{n}(\theta, \varphi)$  of contact  
467 normal between two contacting clumps is obtained based on the spherical coordinate system. The  
468  $P(\vec{n})$  can be obtained according to Eq. 6 below

$$469 \quad P(\vec{n}) = \frac{N_c(d\Omega)}{N_c} \quad (6)$$

470 where  $N_c$  is the total contact number and  $N_c(d\Omega)$  is the contact number of contact normal vectors  
471 pointing in the direction of a range of angle  $d\Omega$ .

472 The  $P(\vec{n})$  measured in the interface zone of the four ISTs at initial state, peak shear stress state, and  
473 steady shear stress state are shown in Fig. 17. The shape of  $P(\vec{n})$  is close to a spherical ball at the  
474 initial state because the specimen is approximately isotropic. As shearing stress increases, the  
475 contact orientation gradually accumulates in a certain direction. The concentration of contact  
476 orientation is a rearrangement process of particles, increasing the material's anisotropy. The  
477 anisotropy at the peak shear stress state is affected by the particle shape, and correspondingly, the  
478 shape of  $P(\vec{n})$  is different. The anisotropy direction for all the tests featuring various  $S$  at peak shear  
479 stress state ranges between  $40^\circ$  and  $60^\circ$ . When the shear stress softening occurs and approaches a  
480 steady state, the decrease of anisotropy results in the reshaping of  $P(\vec{n})$ .



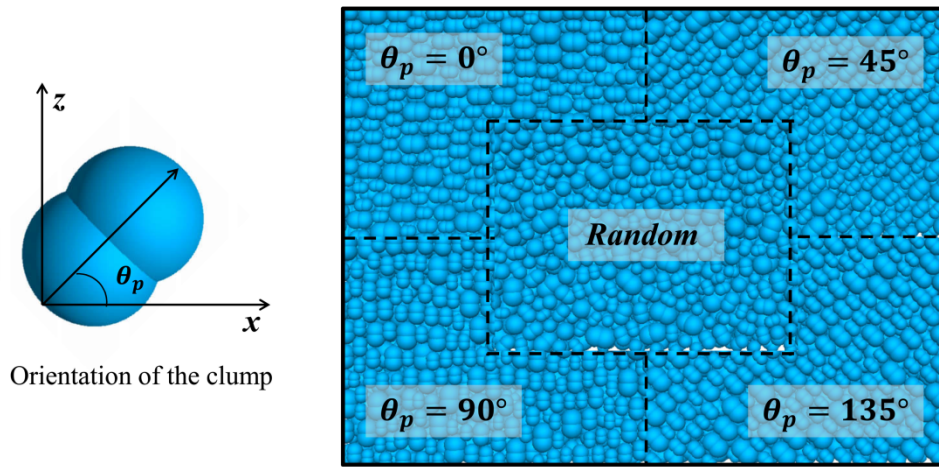
482 Fig. 17. The contact normal distribution in the interface zone of the four ISTs ( $\sigma_n = 50$  MPa,  $R_n =$   
483 0.5) at initial state, peak shear stress state, and steady shear stress state

## 484 **5. Effect of initial fabric**

485 In the previous section, the particles were generated randomly inside the shear box, and  
486 approximately isotropic specimens were produced. However, the initial material fabric depends  
487 upon the initial orientation of the irregular particles, which has an impact on the shearing behavior  
488 of SSI. As shown in Fig. 18,  $\theta_p$  is defined as the included angle between the long axis of the clump  
489 and the shear direction (positive  $x$ -direction). A specimen consisting of 29,058 clumps featuring  
490  $S = 0.7$  with a randomly generated orientation was prepared. In addition, another four specimens  
491 were prepared with a given orientation ( $\theta_p = 0^\circ/45^\circ/90^\circ/135^\circ$ ) for each particle. An approximate  
492 initial porosity  $n_0$  was controlled for all specimens as listed in Table 3. These specimens sheared on  
493 a rough interface featuring  $R_n$  equals 0.5 under a normal stress  $\sigma_n$  equals 25/50/100 MPa.

494 Table 3. Summary of the numerical tests with various initial fabrics

Test	Clump orientation	Initial porosity: $n_0$
IST-a	$\theta_p = 0^\circ$	0.337
IST-b	$\theta_p = 45^\circ$	0.335
IST-c	$\theta_p = 90^\circ$	0.339
IST-d	$\theta_p = 135^\circ$	0.336
IST-e	Random	0.338



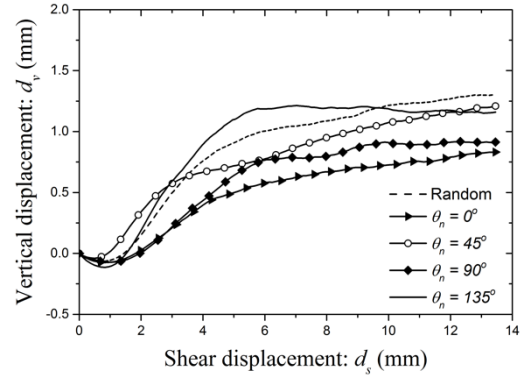
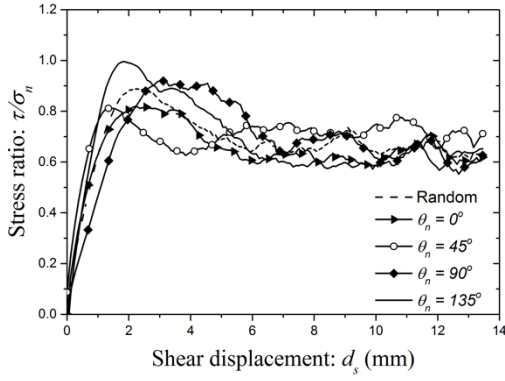
495

496 Fig. 18. Five specimens consisting of clumps ( $S = 0.7$ ) with given orientations

497 **5.1 Macroscopic response**

498 The evolutions of stress ratio  $\tau/\sigma_n$  and vertical displacement  $d_v$  are illustrated in Fig. 19. The peak  
 499 shear stress  $\tau_p$  is affected by the initial orientation of clumps. The specimen consisting of  
 500 horizontally placed clumps ( $\theta_p = 0^\circ$ ) shows the lowest shearing resistance. As the  $\theta_p$  increases, the  
 501 shearing resistance increases. The peak shear stress for the case with randomly distributed clumps is  
 502 between the extreme cases ( $\theta_p = 0^\circ$  and  $\theta_p = 135^\circ$ ). Stress softening is observed among all cases.  
 503 Moreover, the values of  $d_s$  at which the peak shear stress ratio  $\tau_p/\sigma_n$  is achieved are different for  
 504 the five tests. This implies that a different value of  $d_s$  is required to fully trigger the interlocking  
 505 inside the granular materials. Fig. 19b illustrates a similar evolutionary trend of volumetric change  
 506 for various specimens. Before the peak shear stress is achieved, the specimen with an included  
 507 angle  $\theta_p = 135^\circ$  shows the largest dilation; in contrast, the one with horizontally placed clumps  
 508 dilates less than the others. These results suggest that the vertical movement tends to be easily  
 509 triggered when the clumps are randomly placed and  $\theta_p = 135^\circ$ . In contrast, horizontally placing the  
 510 clumps restricts the interaction between the bottom layer clumps and the rough interface.  
 511 Accordingly, both the shear strength and dilatation for that case are the smallest.





512

(a)

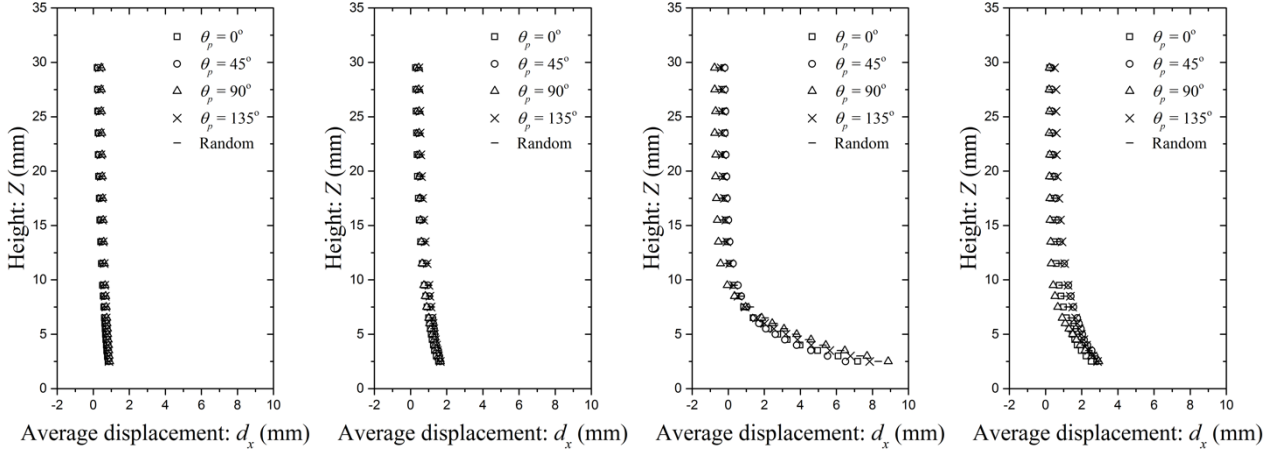
(b)

513

514 Fig. 19. Macro-responses of the ISTs featuring various included angle  $\theta_p$  ( $\sigma_n = 50$  MPa,  $R_n = 0.5$ ):  
 515 (a) stress ratio  $\tau/\sigma_n$  versus shear displacement  $d_s$ ; (b) vertical displacement  $d_v$  versus shear  
 516 displacement  $d_s$

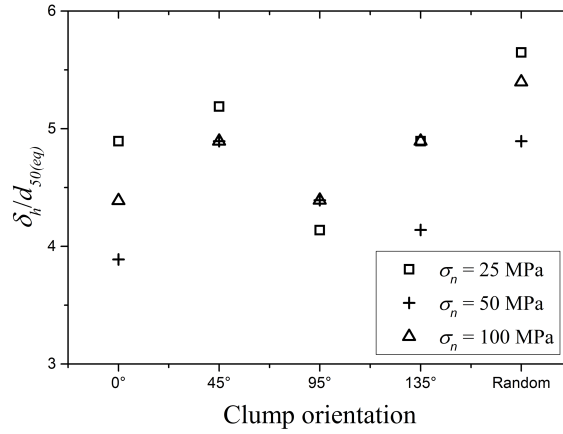
## 517 5.2 Localized band analysis

518 The curves of  $\overline{d_x}$ - $Z$  for the IST-a/b/c/d/e at different shear stress states are plotted in Fig. 20. The  
 519 evolution pattern of  $\overline{d_x}(Z)$  curves is similar to those of ISTs with varying  $S$ . According to the  
 520 analysis of curvature  $\kappa$ , the thickness of the localized band can be obtained. Fig. 21 illustrates the  
 521 normalized thickness  $\delta_h/d_{50(eq)}$  under varying normal stress  $\sigma_n$ , where  $d_{50(eq)}$  is the equivalent  
 522 mean particle diameter. Generally, the  $\delta_h/d_{50(eq)}$  is larger when the specimen subjected to a  
 523 smaller  $\sigma_n$ , because the material dilates more under a lower confining stress. Besides, it shows that  
 524 the  $\delta_h/d_{50(eq)}$  depends on the particle orientation rather than the particle sphericity at the steady  
 525 stress state. A thicker localized band is formed in the specimen with inclined clumps (i.e.  $\theta_p =$   
 526  $45^\circ$  and  $135^\circ$ ) and randomly distributed clumps. It is noted that the value of  $\delta_h/d_{50(eq)}$  varies  
 527 between 4 and 6, which is slightly higher than that ( $\delta_h/d_{50(eq)} = 4$ ) measured from the previous  
 528 tests presented in section 4. This is because the  $n_0$  for these tests are relatively higher than the  
 529 previous ones. The loose specimen tends to form a thicker localized band.



530

531 Fig. 20. Average shear displacement in  $x$ -direction  $\overline{d_x}$  of five ISTs (random distribution,  $\theta_p =$   
 532  $0^\circ/45^\circ/90^\circ/135^\circ$ ) at different strain states: (a)  $d_s = 1.0$  mm; (b)  $d_s = 2.0$  mm; (c)  $d_s = 4.0$  mm;  
 533 and (d)  $d_s = 13.5$  mm



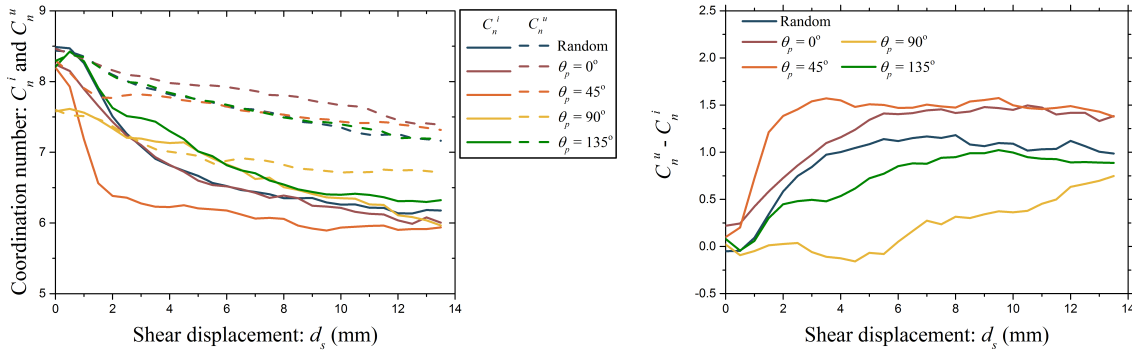
534

535 Fig. 21. The normalized thickness of localized band  $\delta_h/d_{50(eq)}$  of the specimen comprising of  
 536 different orientated particles under varying normal stress  $\sigma_n$

537 **5.3 Local coordination number**

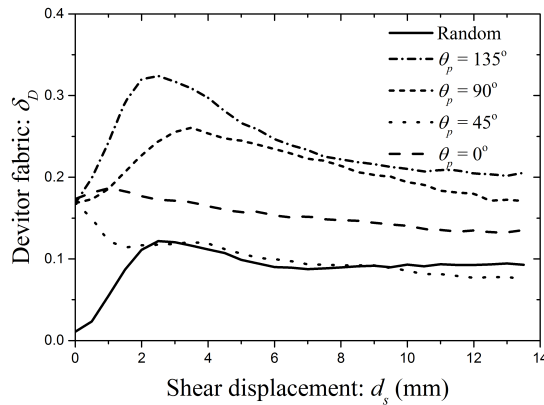
538 The evolutions of coordination number inside the interface zone  $C_n^i$  and the upper zone  $C_n^u$  for the  
 539 five ISTs are illustrated in Fig. 22a. The dilation primarily occurs in the interface zone, which is  
 540 consistent with the tests with varying  $S$  (Fig. 15). On the other hand, the  $C_n^u$  also decreases during

541 the shearing test; especially in the case  $\theta_p = 90^\circ$ , it almost decreased the same as the  $C_n^i$ . Fig. 22b  
 542 shows the difference between the values measured in the interface zone and upper zone  $C_n^u - C_n^i$ .  
 543 The values of  $C_n^u - C_n^i$  increase gradually and approach a steady value. It can be noted that the  
 544 value for case  $\theta_p = 90^\circ$  is quite different from the others because the vertically placed clumps are  
 545 easily disturbed by the shearing even in the upper zone.



546  
 547 Fig. 22. (a) Coordination number inside the interface zone  $C_n^i$  and upper zone  $C_n^u$  of the ISTs ( $\sigma_n =$   
 548 50 MPa) with differently orientated clumps; (b) the difference between the values measured in the  
 549 interface zone and upper zone  $C_n^u - C_n^i$

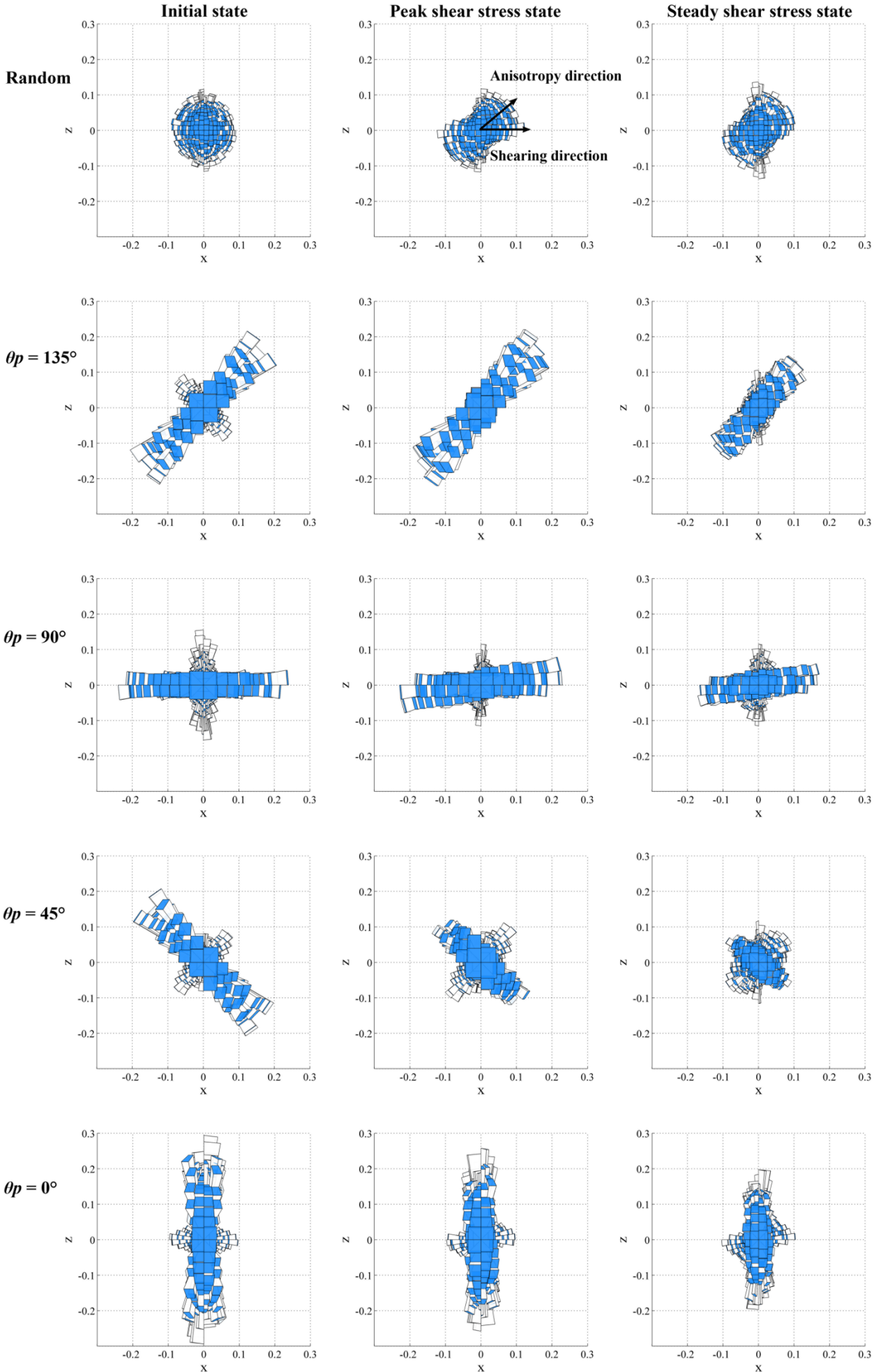
550 **5.4 Material fabric analysis**



551

552 Fig. 23. The evolution of deviator fabric  $\delta_D$  in the interface zone of five ISTs (random,  $\theta_p =$   
553  $0^\circ/45^\circ/90^\circ/135^\circ$ ) under  $\sigma_n = 50$  MPa and  $R_n = 0.5$

554 The evolutions of  $\delta_D$  measured in the interface zone for the ISTs under  $\sigma_n = 50$  MPa are plotted in  
555 Fig. 23, and the  $P(\vec{n})$  at various states are shown in Fig. 24. The specimen consisted of randomly  
556 generated clumps, almost isotropic before shearing. Over the progress of shearing, the contacts  
557 accumulate in a specific direction, correlated with the shear direction. This anisotropy is purely  
558 induced by the shearing, which increases gradually and approaches a peak value at the peak shear  
559 stress state. The shear-induced “anisotropy direction” is shown in the figure of  $P(\vec{n})$ . On the other  
560 hand, the initial fabric of specimens consisting of variously oriented particles is anisotropic since  
561 the contacts initially concentrated in various directions. The initial anisotropic  $\delta_D$  for those  
562 specimens are about 0.17. As the shear displacement  $d_s$  increases, the  $\delta_D$  increases and then  
563 decreases once the stress softening occurs for the cases with  $\theta_p = 0^\circ/90^\circ/135^\circ$ , as well as the case  
564 with a randomly generated specimen. Especially when  $\theta_p = 135^\circ$ , the contact normal has already  
565 been concentrated in the direction of pure shear-induced anisotropy. Thus, the highest level of  
566 anisotropy is observed, and accordingly, the largest shearing stress is measured. By contrast, the  
567 initial contacts ( $\theta_p = 45^\circ$ ) gather in a direction perpendicular to the pure shear-induced anisotropy  
568 direction, preventing the development of the shear-induced anisotropy. For this reason, the  $\delta_D$   
569 decreases continuously, and a minimum peak shear stress is measured. These results demonstrate  
570 that the evolution of  $P(\vec{n})$  of an anisotropic specimen is profoundly correlated with the “shear-  
571 induced anisotropy direction” in the isotropy specimen.



573 Fig. 24. The contact normal distribution in the interface zone of the five ISTs (random,  $\theta_p =$   
574  $0^\circ/45^\circ/90^\circ/135^\circ$ ) under  $\sigma_n = 50$  MPa and  $R_n = 0.5$  at initial state, peak shear stress state, and  
575 steady shear stress state

## 576 **6. Conclusions**

577 The macro- and micro- shearing behaviors of a soil-structural interface have been studied using 3D  
578 DEM simulations of ISTs that feature varying sphericity  $S$  and initial fabric. The effects of  $S$  and  $\sigma_n$   
579 on shear strength, volumetric changes, thickness of the localized band, local porosity, contact  
580 normal distribution, and material fabric anisotropy have been analyzed. The following conclusions  
581 are drawn.

582 (1) Particle sphericity  $S$  plays a significant role in the mechanical properties of the SSI. The shear  
583 strength of the interface (i.e.  $\tau_p/\sigma_n$ ,  $\phi_p$  and  $\phi_s$ ) increases as  $S$  decreases. The volumetric change in  
584 the specimen also depends on  $S$ . A larger dilation is observed for the specimen composed of non-  
585 spherical particles. Anisotropy in the interface zone is increased and a higher deviator fabric  $\delta_D$  is  
586 induced by shearing when  $S$  is smaller.

587 (2) The interface roughness  $R_n$  affects the shearing behavior of interface. The interface friction  
588 angle  $\phi_p$  ascends with the increasing  $R_n$  and reaches to a plateau value. The growing rate is  
589 associated with the particle sphericity  $S$ . A thicker localized band is observed in the IST featuring a  
590 rougher interface.

591 (3) The shear strength of the interface is affected by the initial fabric (particle orientation) of the  
592 specimen. The peak shear stress increases as the particle orientation increases. The initial fabric is  
593 associated with the interaction between the particles and rough interface, i.e., restricts or triggers the  
594 particle motions. The specimen with an inclined angle  $\theta_p = 135^\circ$  shows the largest dilation; in  
595 contrast, the one with horizontally placed clumps dilates less than the others. The thickness of the

596 localized band  $\delta_h$  depends on the initial fabric. A thicker localized band is formed in a specimen  
597 with inclined clumps ( $\theta_p = 45/135^\circ$ ) and randomly distributed clumps.

598 It is noted that this study has only examined the effect of sphericity  $S$  of irregular particles. Particle  
599 shape in nature is more random and complicated. To extend the study, other shape parameters  
600 should be considered in the future. Nevertheless, this study clearly indicates the significant effect of  
601  $S$  and its correlation with interface shear strength. The analysis of the micro-quantities, including  
602 the contact normal distribution, the motion of the particle, and the local porosity distribution,  
603 improves our understanding of the micro-mechanisms associated with soil-interface shearing.

## 604 **Acknowledgement**

605 The authors wish to thank the financial support from the Macau Science and Technology  
606 Development Fund (FDCT) (125/2014/A3), the National Natural Science Foundation of China  
607 (Grant no. 51508585/51678319) and the University of Macau Research Fund (MYRG2017-00198-  
608 FST). This project has received funding from the Marie Skłodowska-Curie Actions Research and  
609 Innovation Staff Exchange programme under grant agreement No [778360].

## 610 **List of Figure**

611 Fig. 1. (a) Definition of the sphericity  $S$  (Krumbein & Sloss 1951); (b) clumps used in this  
612 study

613 Fig. 2. Specimen generation procedure after Muir and Kenichi (2007)

614 Fig. 3. Schematic diagram of interface shear test in the DEM simulation

615 Fig. 4. The extreme porosities  $n_{\max}$  and  $n_{\min}$  of the specimen featuring various sphericity  $S$

616 Fig. 5. Macroscopic responses of the ISTs comprising particles of various  $S$  ( $D_r = 90\%$ ,  $R_n =$   
617  $0.5$ ,  $\sigma_n = 50$  MPa): (a) stress ratio  $\tau/\sigma_n$  versus shear displacement  $d_s$ ; (b) vertical  
618 displacement  $d_v$  versus shear displacement  $d_s$

619 Fig. 6. Macroscopic responses of the ISTs ( $S = 0.5$ ,  $\sigma_n = 50$  MPa) featuring varying  
620 normalized roughness  $R_n$ : (a) stress ratio  $\tau/\sigma_n$  versus shear displacement  $d_s$ ; (b) vertical  
621 displacement  $d_v$  versus shear displacement  $d_s$

622 Fig. 7. (a) Fitting the peak shear stress  $\tau_p$  as a function of normal stress  $\sigma_n$ ; (b) fitting the  
623 steady shear stress  $\tau_s$  as a function of normal stress  $\sigma_n$  ( $R_n = 0.5$ )

624 Fig. 8. (a) Peak friction angle  $\phi_p$  obtained in the DEM ISTs; (b) comparison of the steady  
625 friction angle  $\phi_s$  obtained in the DEM ISTs to the critical friction angle  $\phi_c$  of pure soil  
626 obtained in the laboratory experiments (Cho, Dodds, and Santamarina 2006) at varying  
627 sphericity  $S$

628 Fig. 25. The peak friction angle  $\phi_p$  at varying normalized roughness of interface  $R_n$  and  
629 sphericity  $S$

630 Fig. 26. Comparison of the friction angle ratio  $\phi_p/\phi_p^d$  obtained in the DEM to those measured  
631 in the laboratory experiments (Su et al. 2018; Wu and Yang 2016) at varying normalized  
632 roughness  $R_n$  of interface

633 Fig. 11. Set-up of measuring window at different height  $Z$  of the specimen

634 Fig. 12. Average shear displacement in x-direction  $\overline{d_x}$  of four ISTs ( $R_n = 0.5$ ,  $\sigma_n = 50$  MPa)  
635 at different shear states: (a)  $d_s = 1.0$  mm; (b)  $d_s = 2.0$  mm; (c)  $d_s = 4.0$  mm; and (d)  
636  $d_s = 13.5$  mm

637 Fig. 27. Normalized thicknesses of localized band  $\delta_h/d_{50(eq)}$  of ISTs ( $S = 0.5$ ) at different  
638 normal stress  $\sigma_n$  and interface roughness  $R_n$

639 Fig. 14. Local porosity inside the central section of the specimen ( $R_n = 0.5$ ,  $S = 0.7$ ) at  
640 different strain states: (a)  $d_s = 0.0$  mm; (b)  $d_s = 2.0$  mm; (c)  $d_s = 4.0$  mm; and (d)  $d_s =$   
641  $13.5$  mm

642 Fig. 15. (a) Coordination number inside the interface zone  $C_n^i$  and upper zone  $C_n^u$  of the ISTs  
643 ( $R_n = 0.5$ ,  $\sigma_n = 50$  MPa) with varying sphericity  $S$ ; (b) the difference between the value  
644 measured in interface zone and upper zone  $C_n^u - C_n^i$

645 Fig. 16. The evolution of deviator fabric  $\delta_D$  in the interface zone of the ISTs with various  
646 sphericities  $S = 1.0/0.9/0.7/0.5$  ( $\sigma_n = 50$  MPa,  $R_n = 0.5$ )

647 Fig. 17. The contact normal distribution in the interface zone of the four ISTs ( $\sigma_n = 50$  MPa,  
648  $R_n = 0.5$ ) at initial state, peak shear stress state, and steady shear stress state



- 649 Fig. 18. Five specimens consisting of clumps ( $S = 0.7$ ) with given orientations
- 650 Fig. 19. Macro-responses of the ISTs featuring various included angle  $\theta_p$  ( $\sigma_n = 50$  MPa,  $R_n =$   
651  $0.5$ ): (a) stress ratio  $\tau/\sigma_n$  versus shear displacement  $d_s$ ; (b) vertical displacement  $d_v$   
652 versus shear displacement  $d_s$
- 653 Fig. 20. Average shear displacement in x-direction  $d_x$  of five ISTs (random distribution,  $\theta_p =$   
654  $0^\circ/45^\circ/90^\circ/135^\circ$ ) at different strain states: (a)  $d_s = 1.0$  mm; (b)  $d_s = 2.0$  mm; (c)  $d_s =$   
655  $4.0$  mm; and (d)  $d_s = 13.5$  mm
- 656 Fig. 21. The normalized thickness of localized band  $\delta_h/d_{50(eq)}$  of the specimen comprising of  
657 different orientated particles under varying normal stress  $\sigma_n$
- 658 Fig. 22. (a) Coordination number inside the interface zone  $C_n^i$  and upper zone  $C_n^u$  of the ISTs  
659 ( $\sigma_n = 50$  MPa) with differently orientated clumps; (b) the difference between the values  
660 measured in the interface zone and upper zone  $C_n^u - C_n^i$
- 661 Fig. 23. The evolution of deviator fabric  $\delta_D$  in the interface zone of five ISTs (random,  $\theta_p =$   
662  $0^\circ/45^\circ/90^\circ/135^\circ$ ) under  $\sigma_n = 50$  MPa and  $R_n = 0.5$
- 663 Fig. 24. The contact normal distribution in the interface zone of the five ISTs (random,  $\theta_p =$   
664  $0^\circ/45^\circ/90^\circ/135^\circ$ ) under  $\sigma_n = 50$  MPa and  $R_n = 0.5$  at initial state, peak shear stress  
665 state, and steady shear stress state

## 666 List of Table

- 667 Table 1. Summary of the numerical tests with various elements
- 668 Table 2. Summary of the peak friction angles of ISTs and DSTs
- 669 Table 3. Summary of the numerical tests with various initial fabrics

## 670 Reference

- 671 Ai, J., J.F. Chen, J.M. Rotter, and J.Y. Ooi. 2011. "Assessment of Rolling Resistance Models in  
672 Discrete Element Simulations." *Powder Technology* 206(3): 269–82.
- 673 Barreto, D., C. O'Sullivan, and L. Zdravkovic. 2009. "Quantifying the Evolution of Soil Fabric  
674 under Different Stress Paths." In *AIP Conference Proceedings*, London, 181–84.

- 675 Bono, J.P., and G.R. McDowell. 2015. "An Insight into the Yielding and Normal Compression of  
676 Sand with Irregularly-Shaped Particles Using DEM." *Powder Technology* 271: 270–77.
- 677 Chang, C.S., and Z.Y. Yin. 2009. "Micromechanical Modeling for Inherent Anisotropy in Granular  
678 Materials." *Journal of engineering mechanics* 136(7): 830–39.
- 679 Chen, X., J. Zhang, Y. Xiao, and J. Li. 2015. "Effect of Roughness on Shear Behavior of Red Clay  
680 – Concrete Interface in Large-Scale Direct Shear Tests." *Canadian Geotechnical Journal*  
681 52(8): 1122–35.
- 682 Cho, G.C., J. Dodds, and J.C. Santamarina. 2006. "Particle Shape Effects on Packing Density ,  
683 Stiffness and Strength: Natural and Crushed Sands." *Journal of Geotechnical and*  
684 *Geoenvironmental Engineering* 132(5): 591–602.
- 685 Coetzee, C.J. 2016. "Calibration of the Discrete Element Method and the Effect of Particle Shape."   
686 *Powder Technology* 297: 50–70.
- 687 Cundall, P.A., and O.D.L. Strack. 1979. "A Discrete Numerical Model for Granular Assemblies."   
688 *Géotechnique* 29(1): 47–65.
- 689 Dejong, J.T., D. White, and M.F. Randolph. 2006. "Microscale Observation and Modeling of Soil-  
690 Structure Interface Behavior Using Particle Image." *Soils and Foundations* 46(1): 15–28.
- 691 Frost, J.D., J.T. Dejong, and M. Recalde. 2002. "Shear Failure Behavior of Granular-Continuum  
692 Interfaces." *Engineering Fracture Mechanics* 69(17): 2029–48.
- 693 Hossain, M.A., and J.H. Yin. 2014. "Behavior of a Pressure-Grouted Soil-Cement Interface in  
694 Direct Shear Tests." *International Journal of Geomechanics* 14(1): 101–9.
- 695 Hu, L.M., and J.L. Pu. 2005. "Testing and Modeling of Soil-Structure Interface." *Journal of*  
696 *Geotechnical and Geoenvironmental Engineering* 130(8): 851–60.
- 697 Iwashita, K., and M. Oda. 1998. "Rolling Resistance at Contacts in Simulation of Shear Band  
698 Development by DEM." *Journal of Engineering Mechanics* 124(3): 285–92.
- 699 Jensen, R.P., P.J. Bosscher, M.E. Plesha, and T.B. Edil. 1999. "DEM Simulation of Granular  
700 Media-Structure Interface: Effects of Surface Roughness and Particle Shape." *International*  
701 *Journal for Numerical and Analytical Methods in Geomechanics* 23(6): 531–47.

- 702 Jiang, M., and Z.Y. Yin. 2012. "Analysis of Stress Redistribution in Soil and Earth Pressure on  
703 Tunnel Lining Using the Discrete Element Method." *Tunnelling and Underground Space*  
704 *Technology* 32: 251–59.
- 705 Jiang, Mingjing, and Z.Y. Yin. 2014. "Influence of Soil Conditioning on Ground Deformation  
706 during Longitudinal Tunneling." *Comptes Rendus Mecanique* 342(3): 189–97.
- 707 Jing, X.Y. et al. 2017. "Analysis of Soil-Structural Interface Behavior Using Three-Dimensional  
708 DEM Simulations." *International Journal for Numerical and Analytical Methods in*  
709 *Geomechanics* 42(2): 339–57.
- 710 Jing, X.Y., W.H. Zhou, and Y.M. Li. 2017. "Interface Direct Shearing Behavior between Soil and  
711 Saw-Tooth Surfaces by DEM Simulation." In *Procedia Engineering*, Delft, The Netherlands,  
712 36–42.
- 713 Krumbein, W.Ch., and L.L. Sloss. 1951. *Stratigraphy and Sedimentation*. LWW.
- 714 Lin, X., and T.T. Ng. 1997. "A Three-Dimensional Discrete Element Model Using Arrays of  
715 Ellipsoids." *Géotechnique* 47(2): 319–29.
- 716 Lu, M., and G.R. McDowell. 2007. "The Importance of Modelling Ballast Particle Shape in the  
717 Discrete Element Method." *Granular matter* 9(1–2): 69–80.
- 718 Mindlin, R.D., and H. Deresiewicz. 1953. "Elastic Spheres in Contact under Varying Oblique  
719 Forces." *Journal of Applied Mechanics* 20: 327–44.
- 720 Miura, K., K. Maeda, M. Furukawa, and S. Toki. 1998. "Mechanical Characteristics of Sands with  
721 Different Primary Properties." *Soils and Foundations* 38(4): 159–72.
- 722 Nakata, Y. et al. 2001. "One-Dimensional Compression Behaviour of Uniformly Graded Sand  
723 Related to Single Particle Crushing Strength." *Soils and Foundations* 41(2): 39–51.
- 724 Ni, Q., W. Powrie, X. Zhang, and R. Harkness. 2000. "Effect of Particle Properties on Soil  
725 Behavior: 3-D Numerical Modeling of Shearbox Tests." In *Numerical Methods in*  
726 *Geotechnical Engineering*, ASCE Geotechnical Special Publication, 58–70.
- 727 Ochiai, H., J. Otani, S. Hayashic, and T. Hirai. 1996. "The Pull-out Resistance of Geogrids in  
728 Reinforced Soil." *Geotextiles and Geomembranes* 14(1): 19–42.

- 729 Oda, M., S. Nemat-Nasser, and J. Konishi. 1985. "Stress-Induced Anisotropy in Granular Masses."  
730 *Soils and foundations* 25(3): 85–97.
- 731 Paikowsky, S.G., C.M. Player, and P.J. Connors. 1995. "A Dual Interface Apparatus for Testing  
732 Unrestricted Friction of Soil along Solid Surfaces." *ASTM geotechnical testing journal* 18(2):  
733 168–93.
- 734 Rao, K.S.S., M.M. Allam, and R.G. Robinson. 1998. "Interfacial Friction between Sands and Solid  
735 Surfaces." In *Proceedings of the ICE - Geotechnical Engineering*, , 75–82.
- 736 Rothenburg, L., and R.J. Bathurst. 1992. "Micromechanical Features of Granular Assemblies with  
737 Planar Elliptical Particles." *Géotechnique* 42(1): 79–95.
- 738 Salot, C., P. Gotteland, and P. Villard. 2009. "Influence of Relative Density on Granular Materials  
739 Behavior: DEM Simulations of Triaxial Tests." *Granular matter* 11(4): 221–36.
- 740 Santamarina, J.C., and G.C. Cho. 2004. "Soil Behaviour: The Role of Particle Shape." In *Advances*  
741 *in Geotechnical Engineering: The Skempton Conference*, London, 604–17.
- 742 Satake, M. 1992. "A Discrete-Mechanical Approach to Granular Materials." *International journal*  
743 *of engineering science* 30(10): 1525–33.
- 744 Su, L.J., J.H. Yin, and W.H. Zhou. 2010. "Influences of Overburden Pressure and Soil Dilation on  
745 Soil Nail Pull-out Resistance." *Computers and Geotechnics* 37(4): 555–64.
- 746 Su, L.J., W.H. Zhou, W.B. Chen, and X. Jie. 2018. "Effects of Relative Roughness and Mean  
747 Particle Size on the Shear Strength of Sand-Steel Interface." *Measurement* 122: 339–46.
- 748 Uesugi, M., and H. Kishida. 1986a. "Frictional Resistance at Yield between Dry Sand and Mild  
749 Steel." *Soils and Foundations* 26(4): 139–49.
- 750 ———. 1986b. "Influential Factors of Friction between Steel and Dry Sands." *Soils and*  
751 *Foundations* 26(2): 33–46.
- 752 Uesugi, M., H. Kishida, and Y. Tsubakihara. 1988. "Behavior of Sand Particles in Sand-Steel  
753 Friction." *Soils and Foundations* 28(1): 107–18.

- 754 Wang, J., M.S. Gutierrez, and J.E. Dove. 2007. "Numerical Studies of Shear Banding in Interface  
755 Shear Tests Using a New Strain Calculation Method." *International Journal for Numerical  
756 and Analytical Methods in Geomechanics* 31(12): 1349–66.
- 757 Wang, J., and M. Jiang. 2011. "Unified Soil Behavior of Interface Shear Test and Direct Shear Test  
758 under the Influence of Lower Moving Boundaries." *Granular Matter* 13(5): 631–41.
- 759 Wensrich, C.M., and A. Katterfeld. 2012. "Rolling Friction as a Technique for Modelling Particle  
760 Shape in DEM." *Powder Technology* 217: 409–17.
- 761 Wood, D.M., and K. Maeda. 2007. "Changing Grading of Soil : Effect on Critical States." *Acta  
762 Geotechnica* 3(1): 3–14.
- 763 Wu, X.Y., and J. Yang. 2016. "Direct Shear Tests of the Interface between Filling Soil and Bedrock  
764 of Chongqing Airport." In *Advances in Civil, Environmental, and Materials Research  
765 (ACEM16)*, Jeju Island, Korea.
- 766 Yin, J.H., and W.H. Zhou. 2009. "Influence of Grouting Pressure and Overburden Stress on the  
767 Interface Resistance of a Soil Nail." *Journal of Geotechnical and Geoenvironmental  
768 Engineering* 135(9): 1198–1208.
- 769 Yin, Z.Y., C.S. Chang, and P.Y. Hicher. 2010. "Micromechanical Modelling for Effect of Inherent  
770 Anisotropy on Cyclic Behaviour of Sand." *International Journal of Solids and Structures*  
771 47(14): 1933–51.
- 772 Zhao, L.S., W.H. Zhou, and K.V. Yuen. 2017. "A Simplified Axisymmetric Model for Column  
773 Supported Embankment Systems." *Computers and Geotechnics* 92: 96–107.
- 774 Zhou, W.H., and J.H. Yin. 2008. "A Simple Mathematical Model for Soil Nail and Soil Interaction  
775 Analysis." *Computers and Geotechnics* 35(3): 479–88.
- 776 Zhou, W.H., J.H. Yin, and C.Y. Hong. 2011. "Finite Element Modelling of Pullout Testing on a  
777 Soil Nail in a Pullout Box under Different Overburden and Grouting Pressures." *Canadian  
778 Geotechnical Journal* 48(4): 557–67.
- 779 Zhou, W.H., K.V. Yuen, and F. Tan. 2013. "Estimation of Maximum Pullout Shear Stress of  
780 Grouted Soil Nails Using Bayesian Probabilistic Approach." *International Journal of  
781 Geomechanics* 13(5): 659–64.

782 Zhu, H.X., W.H. Zhou, and Z.Y. Yin. 2017. "Deformation Mechanism of Strain Localization in 2D  
783 Numerical Interface Tests." *Acta Geotechnica*: 1–17.

784